THE SEA: THE SCIENCE OF OCEAN PREDICTION
Journal of Marine Research, 75, 641–682, 2017

Ocean dynamics

by Gregg Jacobs[1,2] and Baylor Fox-Kemper[3]

ABSTRACT

Operational prediction systems must balance conflicting considerations involved in representing the widest possible range of ocean physics, limited by computational constraints. Choices must be made in prediction systems that exclude particular dynamics to enable feasible solutions within defined resources. We examine some of the basic ocean dynamics that ocean prediction systems intend to represent. The two most basic simplifications are the Boussinesq and hydrostatic. Even with these limitations, ocean models represent a vast range of physical processes, and this enables application to many problems. We examine a succinct range of basic dynamics and consider how these affect operational ocean prediction problems.

Keywords: Operational, ocean, prediction, dynamics, internal wave, mesoscale, Rossby wave, Kelvin wave

1. Introduction

We observe the ocean and find it contains features covering immense ranges of scale (Figure 1). All these features are subjects of operational ocean predictions, and the underlying dynamics determine choices in the development of operational systems. Therefore, the purpose at hand is to examine some of the fundamental dynamics and considerations with respect to operational ocean prediction systems.

At the largest scale, in the North Atlantic as heat leaves the ocean, water sinks to the abyss flowing southward to the Antarctic Circumpolar current to resurface and warm as it moves to the north again, making a 15,000 km trip spanning nearly half of the Earth's circumference. This is one important branch of the global overturning circulation. In the subtropical region depicted in Figure 1, strong westerly wind stress on the poleward side of this domain and easterly wind stress to its south drive a basin-wide (6,000 km zonally, 3,500 km meridionally) anticyclonic (clockwise in the Northern Hemisphere) subtropical

1. Naval Research Laboratory, 1009 Balch Blvd, Stennis Space Center, MS 39529
2. Corresponding author: ***e-mail: gregg.jacobs@nrlssc.navy.mil***
3. Brown University, Department of Earth, Environmental, and Planetary Sciences, 324 Brook Street, Providence, RI 02912; ***e-mail: Baylor_Fox-Kemper@brown.edu***

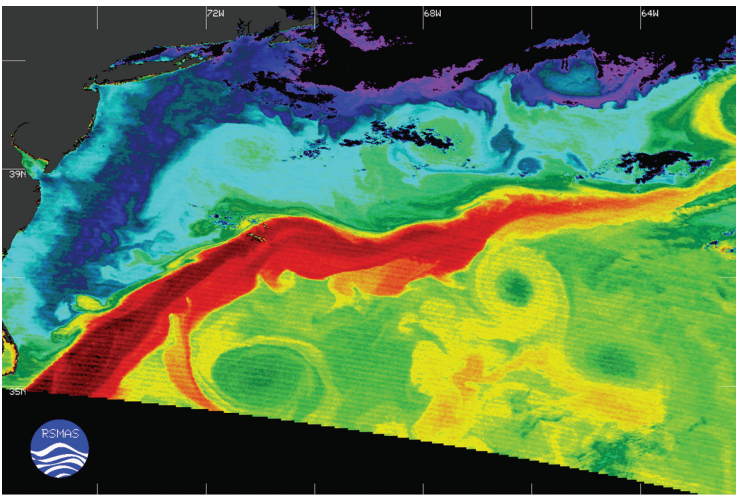

Figure 1. A sea surface temperature image from the moderate-resolution imaging spectroradiometer (MODIS) on 8 May 2000. An enormous range of scales exists. The Gulf Stream is the red warm waters entering from the southwest. This western boundary current is part of the North Atlantic subtropical gyre basin circulation. Instabilities in the Gulf Stream generate large, circular mesoscale eddies to the north as warm core rings and to the south as cold core rings. Along many of the temperature fronts are filaments, and in the northern area there are smaller instabilities due to submesoscale eddies. The continental shelf waters are distinct from the cold water flowing south from the Labrador Sea. Warmer waters are observed in the Hudson River outlet. Image credit: Earth Observatory, NASA.

gyre circulation. The most conspicuous feature of this gyre is the western boundary current, which is the 30–150 Sv Gulf Stream in this basin and the 24 Sv Kuroshio in North Pacific. Poleward of the subtropical gyres, cyclonic (counter-clockwise in the Northern Hemisphere) subpolar gyres are the oceanic response to strong westerly winds on their equatorward side and weaker winds poleward. The colder waters of the subpolar gyre are the cooler colors within Figure 1. The wind-driven gyres have a subsurface expression that also plays a role in the overturning circulation. On the 100 km scale, mesoscale eddies are generated through barotropic and baroclinic instabilities and transport heat and water masses. These eddies contain most of the kinetic energy in large-scale oceanic motions—even more than the gyres and meridional overturning. On the 1–10 km scale, submesoscale filaments wrap around the mesoscale eddies, and submesoscale eddies fill the surface waters forming within boundary layers or from strong flows over topographic features. Tidal cycles drive a range of waves that flush waters in bays and estuaries, and these tides interact with topography to create internal wave energy beams that radiate across the ocean basins—sometimes breaking and producing turbulence. On the 0.1–100 m scales, turbulence and surface waves fill the upper ocean, mixing water properties and affecting the exchange of energy, momentum,

freshwater, and gasses with the atmosphere. Occasionally, seismic activity may trigger a tsunami that travels at hundreds of meters per second, perturbing the whole 3.7 km deep ocean as it passes.

All these processes are of importance to operational ocean prediction. A key characteristic of operational ocean predictions is that they are produced on a scheduled basis. The frequency of predictions varies depending on the application. Storm surge forecasting across coasts and within estuaries can require several predictions per day depending on the frequency with which more accurate atmospheric wind forecasts are updated. Ocean general circulation forecasts are typically updated once per day as observations help constrain the positions of ocean features such as eddies. Hypoxia forecasts are conducted seasonally to annually in the process of setting policies that can affect the use of upstream fertilizers. The Intergovernmental Panel on Climate Change (IPCC) projections are constructed every six years on average with the intent to define trends and statistical ranges of mean and extreme events. Although the IPCC projections and purposes are different from operational forecasts, the underlying conflict between representation of dynamics and finite computational capability exist.

The common characteristic amongst these is the need for a forecast as accurate as possible at a fixed time. That is, there is a deadline at which the forecast must be provided in order for decisions to be made. The decisions include determination of evacuation from coastal flooding, where to send fishing fleets on a daily basis, management policies for the upcoming year, and efforts toward defining long term policies for climate change. The imposed forecast deadline implies that a fixed computational capability may be applied to the problem. The accurate forecast implies inclusion of complex physics at all scales, which leads to a computationally intractable problem. As a simple example, the problem of forecasting drift for search and rescue or hazard mitigation must take into account wind forcing, the development of waves, the transfer of momentum into the ocean and its distribution within the surface, solar radiation that will change stratification and the ability for momentum to mix into the ocean, the development of surface ageostrophic flows from Langmuir cells, the transport of submesoscale and mesoscale eddies, and trends in the global circulation. The ability to directly incorporate all the dynamical processes into a single system that will provide a forecast is limited by available computers—forecasts featuring full resolution of all oceanic processes (direct numerical simulation) are still centuries away given present rates of computational improvement (Fox-Kemper et al. 2014). Thus, the need for an accurate forecast and the inclusion of as many phenomena as possible, while still arriving at the imposed deadline, are competing forces.

Researchers developing operational forecast systems must balance these requirements. Such a balance implies consideration of the relevant dynamical processes at work. The most influential processes must be directly represented by numerical models, whereas others may be parameterized (See discussion in Haidvogel et al., in press). Thus, the purpose within this chapter is to introduce the dynamical processes typically represented in ocean circulation models, along with their scales and scaling laws, that can be used to estimate

their importance. This information provides the basis on subsequent decisions in designing operational forecast systems.

2. The basic governing equations

The starting point for understanding ocean dynamics are the fundamental equations governing fluid mechanics based on conservation of properties. A common convention, which is used here, is that the (x, y, z) coordinate describes a local reference frame that is positive in the eastward, northward, and increasing geopotential (outward from Earth center). However, note that vectors pointing northward at different points on the surface of the earth are not parallel, likewise for eastward vectors and vectors that indicate the direction of greatest geopotential increase. Thus, to make this convenient convention useful, the limit where the excursions of fluid parcels, L, are restricted to a small fraction of the Earth's circumference, $L \ll 2\pi r_e$, and vertical excursions are restricted to a small fraction of the distance from the Earth's center of mass, $H \ll r_e$ allows the curvature of the earth to be approximated simply while retaining Cartesian coordinates. It may be more convenient to use spherical coordinates when the scales of excursion are large, e.g., the overturning circulation and gyres. Note that our choice of coordinates does not change the fluid dynamics involved, but some coordinate systems are considerably more convenient for particular applications or numerical implementation.

In a Cartesian coordinate we write the conservation equations taking into account non-conservative terms appearing on the right-hand side of the equations. Using this, the rotating Navier–Stokes equations for seawater momentum, seawater mass, and salt mass are

$$\frac{\partial \rho u_i}{\partial t} + 2\rho\Omega_j \varepsilon_{ijk} u_k + \frac{\partial}{\partial x_j}\left(\rho u_i u_j + p\delta_{ij}\right) = \frac{\partial}{\partial x_j}\left(\tau_{ij}\right) + \frac{\partial}{\partial x_i} F_i \tag{1}$$

$$\frac{\partial \rho}{\partial t} + \frac{\partial}{\partial x_j}\left(\rho u_j\right) = 0 \tag{2}$$

$$\frac{\partial \rho S}{\partial t} + \frac{\partial}{\partial x_j}\left(\rho S u_j\right) = \frac{\partial}{\partial x_j} \kappa \frac{\partial \rho S}{\partial x_j} \tag{3}$$

where the deviatoric stress tensor on the right side of the conservation of momentum (equation 1) assumes an isotropic Newtonian fluid

$$\tau_{ij} = \mu\left(\frac{\partial u_i}{\partial x_j} + \frac{\partial u_k}{\partial x_i} - \frac{2}{3}\delta_{ij}\frac{\partial u_k}{\partial x_k}\right) \tag{4}$$

These are presented in a compact tensor notation where u_i is the velocity in the i direction of a local (x, y, z) coordinate, S is the absolute salinity, ρ is the fluid density, τ_{ij} is the stress in the i direction on a plane with perpendicular in the j direction, p is the pressure, μ is the fluid viscosity, Ω_j is the Earth rotation vector, and F_i is the potential representing gravitation, Coriolis and centrifugal forces, and tidal potential. Einstein summation is implied, which

means that any repeated index implies a sum of that term with that index taking each of the three directions in turn. The form of the equations is referred to as a flux form, because each term in the equation is written as a divergence of a flux. The horizontal gradient $\partial/\partial x_j$ of the terms represents the net flux of momentum, stress, and pressure at a given location. Many books cover the derivation of equations (1) and (2) (Gill 1982; Pedlosky 2013; Pope 2001; Vallis 2006). These equations describe the evolution of the vast array of processes observed in the ocean from the global conveyor belt circulation to turbulent dissipation.

The first law of thermodynamics may be written in terms of the enthalpy h following McDougall et al. (2003).

$$\frac{\partial \rho h}{\partial t} + \frac{\partial}{\partial x_i}(\rho h u_i) - \frac{D\rho}{Dt} = \frac{\partial F_j^Q}{\partial x_j} + \rho\varepsilon \tag{5}$$

In the isentropic limit (where irreversible processes are neglected and the greater than symbol becomes an equality), this is

$$\frac{\partial \rho\eta}{\partial t} + \frac{\partial}{\partial x_i}(\rho\eta u_i) \geq -\frac{1}{T}\frac{\partial F_j^Q}{\partial x_j} \tag{6}$$

Where h is enthalpy, F^Q is energy flux by nonadvective processes, ε is kinetic energy dissipation, and η is entropy. Finally, the equation of state provides sufficient equations for a closed system

$$\rho = \rho(h, S, p) \quad \text{or} \quad \rho = \rho(\eta, S, p) \tag{7}$$

A detailed presentation of seawater dynamics is beyond the present scope, but an excellent review is provided by Feistel (2008).

3. Boussinesq approximation

To understand the ocean dynamics throughout this chapter, we will introduce simplifications to the equations. The first of these is the Boussinesq approximation, which relies on density variations having small impact on inertia but having substantial influence when multiplied by gravity. This approximation removes seawater compressibility effects, and therefore the equations moving forward do not represent the propagation of acoustic energy through the ocean. Retaining these effects would require numerical model time steps that are exceedingly small or advanced numerics to handle sound waves. For operational acoustic applications, ocean forecasts provide temperature and salinity from which sound speed is determined, and operational centers then produce separate acoustic propagation forecasts. Thus, the Boussinesq assumption does not remove significant processes that affect operational ocean forecasts, and acoustic forecast capability is not lost.

Density is separated into three components: a global mean value, a global average vertical variability, and deviations from these. Buoyancy is also separated according to

$$\rho = \rho_o + \bar{\rho}\,(z) + \rho'\,(x, y, z, t) = \rho_o \left(1 - \frac{\bar{b}\,(z) + b'\,(x, y, z, t)}{g}\right), \quad N^2 = \frac{\partial \bar{b}}{\partial z} \tag{8}$$

where density and buoyancy are related by $b = -g\rho/\rho_o$, and N is the Brunt–Väisälä frequency, to which we will return shortly. Under this approximation, we can easily relate the flux form to the material derivative, as conservation of mass (2) reduces to the nondivergence requirement $\partial u_j/\partial x_j \approx 0$, and thus

$$\frac{\partial \rho u_i}{\partial t} + \frac{\partial}{\partial x_j}\left(\rho u_i u_j\right) \approx \rho_o \frac{Du_i}{Dt} = \rho_o \left(\frac{\partial}{\partial t} + u_j \frac{\partial}{\partial x_j}\right) u_i \tag{9}$$

Using this relationship, equations (1–3) and (6) provide the closed set of Boussinesq equations of fluid motion as

$$\frac{Du_i}{Dt} + 2\Omega_j \varepsilon_{ijk} u_k = -\frac{1}{\rho_o}\frac{\partial p}{\partial x_i} + \frac{\rho g_i}{\rho_o} + \frac{\partial}{\partial x_j}\nu \frac{\partial u_i}{\partial x_j} \tag{10}$$

$$\frac{\partial u_j}{\partial x_j} = 0 \tag{11}$$

$$\frac{DS}{Dt} = \frac{\partial}{\partial x_j}\kappa \frac{\partial S}{\partial x_j} \tag{12}$$

$$\frac{D\Theta}{Dt} \approx \frac{\theta}{TC_p^0}\frac{\partial F_j^Q}{\partial x_j} \approx \frac{1}{C_p^0}\frac{\partial F_j^Q}{\partial x_j}, \quad \text{or} \quad \frac{D\Theta}{Dt} \approx \frac{\theta}{TC_p\,(p_r)}\frac{\partial F_j^Q}{\partial x_j} \approx \frac{1}{C_p\,(p_r)}\frac{\partial F_j^Q}{\partial x_j} \tag{13}$$

In these, $\nu = \mu/\rho_o$ is the kinematic viscosity. Note that absolute temperatures T, Θ are to be used (i.e., Kelvin not Celsius), which means that setting the temperature ratios to unity is only an O(0.15%) error.

Working from the enthalpy form of the first law of thermodynamics, the highly accurate conservative temperature Θ conservation equation results. The conservative temperature is proportional to the enthalpy that a fluid parcel would take after an adiabatic relocation to the surface (h_o, the potential enthalpy). Conservative temperature is just the potential enthalpy divided by the surface specific heat capacity ($\Theta = h_o/C_p^0$). To good accuracy, the potential temperature based on a nearby reference pressure p_r can be used, which may be derived from conservation of entropy ($D\eta/Dt = C_p(p_r)D\ln\theta/Dt$). Potential temperature is less accurate than conservative temperature, because it also relies on the assumption of conserved entropy during the relocation of the fluid parcel to the surface. In the real world, mixing commonly occurs, which is an irreversible process that increases entropy. Thus, the additional assumption of isentropic relocations renders the potential temperature less accurate. The in situ temperature is not conserved following fluid motion because of compressive heating and expansive cooling, so its use in ocean models is limited.

These equations describe the motions within the fluid, but the ocean is also connected to other parts of the earth system. These connections include warming by the sun, heat exchange with the atmosphere, precipitation, evaporative removal of freshwater leaving saltier, colder water behind, wind stresses, river flows, freezing into ice with rejection of brine, etc. These exchanges are included through boundary conditions that are required for full solutions of the previous equations.

One simplification has already been included. The Earth rotation centrifugal and tidal forces that were in $\partial F_i/\partial x_i$ of (1) are included together into an effective gravitational force g_i within (10). This simplification is convenient and accurate when working with coordinate systems that use geopotential height as a vertical coordinate, which is simple and accurate under the local Cartesian coordinates or spherical coordinates so long as deviations in the geoid are smooth (as they always are on Earth). Note that the earth's surface is closer to an oblate spheroid than a sphere because of the centrifugal force, but it is convenient and accurate to use spherical coordinates and approximate the geoid as a level surface. Vallis (2006) notes that it is critical to approximate the geoid in this way in spherical coordinates, otherwise everything would just roll down toward the equator under an unbalanced centrifugal force!

4. Scaling the equations

Under almost every oceanographic problem of interest, these equations are too difficult to solve directly. To make manipulation of the equations easier, two changes are routine. First, these equations are scaled to determine which terms may be negligible. If they are determined to be so small that they are negligible for the problem at hand, then—mathematical necessity allowing—they can be dropped from the equation set.

McWilliams (1985) presents a scaling for the dimensionless equations of motion for a Boussinesq fluid. We adapt these equations to the purposes here. As different terms are neglected in following sections, the reader can refer back to these equations to better understand what scaling relationships are implied by these assumptions. It is assumed that the typical scales of variables can be characterized by

$$x, y \sim L, \quad z \sim H, \tag{14}$$

$$v \sim V, \quad t \sim L/V, \tag{15}$$

$$\pi = p/\rho_o \sim \max\left[V f_o L, V^2\right] = V f_o L M_R \tag{16}$$

$$b \sim V f_o \frac{L}{H} M_R \tag{17}$$

$$N^2(z) \sim N_o^2 \tag{18}$$

$$\frac{db}{dz} \sim N_o^2 \tag{19}$$

$$w \sim \pi V/N^2 HL = V^2 f_o L M_R/\left(N_o^2 LH\right) \tag{20}$$

$$f = f_o\left(1 + \frac{\beta y}{f_o}\right), \quad \beta = 2\Omega\cos\theta/r_e \tag{21}$$

Where $M_R = \max[1, R_o]$, $R_o = V/f_o L$, f is the Coriolis parameter with a value of f_o at the central latitude and varies linearly with latitudinal distance with a value of β. With these scaling definitions, the horizontal momentum, vertical momentum, density or buoyancy, and mass conservation equations take the dimensionless form:

$$R_o\left(\frac{\partial V_H}{\partial t} + V_H\cdot\nabla V_H + Fr^2 M_R w\frac{\partial V_H}{\partial z}\right) + M_R\nabla_H\pi + \left(1 + \frac{\beta y}{f_o}\right)\mathbf{k}\times\mathbf{V}_H = \frac{R_o}{R_e}\nabla^2\mathbf{V}_H \tag{22}$$

$$Fr^2\frac{H^2}{L^2}\left(\frac{\partial w}{\partial t} + \mathbf{V}_H\cdot\nabla w + Fr^2 M_R w\frac{\partial w}{\partial z}\right) + \frac{\partial\pi}{\partial z} - b = \frac{R_o}{R_e}\nabla^2\mathbf{V}_h \tag{23}$$

$$\frac{\partial b}{\partial t} + \mathbf{V}_H\cdot\nabla b + Fr^2 M_R w\frac{\partial b}{\partial z} + w\frac{N^2}{N_o^2} = 0 \tag{24}$$

$$\nabla\cdot\mathbf{V}_H + Fr^2 M_R\frac{\partial w}{\partial z} = 0 \tag{25}$$

By these definitions, the Rossby number is $R_o = V/f_o L$, the Froude number is $Fr = V/N_o H$, and the Reynolds number is $R_e = \rho_o V L/\mu$. These serve for purposes here, though in many applications other definitions arise based on the choice of scales or dominance of particular balances. For example, when considering the vorticity equations arising from (22), another source for estimating the Rossby number is the geostrophic flow vorticity relative to the reference frame rotating with Earth $\zeta_g = \partial v_g/\partial x - \partial u_g/\partial y$, which is twice the solid body rotation rate of the material. The ratio of ζ_g to the Coriolis parameter provides another form of the Rossby number $R_o = \zeta_g/f_o$ that is the ratio of the fluid to Earth rotation rates.

5. Hydrostatic approximation

The equations of motion (22–25) are the primitive equations and describe the vast range of processes within the ocean. At this point it is necessary to consider the operational application and associated dynamical processes. The hydrostatic assumption implies that the vertical momentum equation (23) reduces to a balance between vertical pressure gradient and gravitational force,

$$\partial p/\partial z = -g\rho \tag{26}$$

This is typically true if $Fr^2 H^2/L^2 = V^2/N_o^2 L^2$ is small and if the ratio of Rossby number to Reynolds number is small. This may also be viewed as a requirement that the frequency

of the flow given by V^2/L^2 be much smaller than the Brunt–Väisälä frequency (Marshall et al. 1997).

Given the decomposition of density in (8), under the hydrostatic assumption we can define a mean vertical pressure profile that complements the mean density profile so that pressure is decomposed by $p = \bar{p}(z) + p'(x, y, z, t)$ with $\partial \bar{p}/\partial z = -g\bar{\rho}$. Be cautious; as the relation between $\bar{p}$ and $\bar{\rho}$ is hydrostatic by the definition, it does not necessarily imply that p' and ρ' are in hydrostatic balance. However, we do expect hydrostatic balance for all small Froude number, small aspect ratio motions.

Computing pressure in a hydrostatic model is very efficient, as it is a diagnosed value according to the hydrostatic approximation. Hydrostatic models enable substantial reduction in operational solution time. Retaining all the terms in (23) requires application of a nonhydrostatic model. Solving the pressure field of the full momentum equations requires substantially greater computational resources and thus a longer solution time. Many very important processes require nonhydrostatic dynamics to resolve. One example is convective processes generated by ocean surface cooling. The outward flux of heat reduces temperature and increases density. Once the buoyancy is less than surrounding waters, a surface water parcel experiences a downward acceleration, and the vertical velocity rate of change is determined by the vertical momentum equation (23). Langmuir cells result from vorticity tilting due to surface wave Stokes drift. The vertical momentum advection is a critical part of the process (Craik and Leibovich 1976). Tidal flow across sharp topography displaces isotherms vertically and results in the generation of internal waves. Large amplitude internal waves steepen while propagating, which must be captured by including nonhydrostatic physics in prediction systems (Zhang, Fringer, and Ramp 2011). The hydrostatic approximation removes these mechanisms, and achieving reasonable results requires representing the processes through parameterization in turbulence schemes that represent the effects of mixing (see Haidvogel et al., in press).

Some parameterizations are as simple as elevating the values of the viscosity and diffusivity used—in effect, this treats turbulent eddies as though they behave just like the molecules in a fluid in terms of diffusing heat and momentum. Under such an approximation, the normally negligible terms involving the very large Reynolds numbers occurring in oceanic flows may be preserved with a different coefficient. Because such terms may be required mathematically, this approach is often useful numerically. Separating resolved and unresolved scales in the equations of motion leads to Reynolds averaging. Equations very similar to the primitive equations (22–25) govern the resolved flow, and second order equations govern the development of the statistics of the unresolved turbulence (Mellor and Yamada 1982; Kantha and Clayson 1994). Such complex closure schemes evolve the parameterized turbulence while taking into account stratification and shear of the large-scale flow. For example, it is easier to mix along density surfaces in the ocean because no mass must be lifted against gravity in the process (Fox-Kemper and Menemenlis 2008). In contrast, mixing across density surfaces against gravity requires energy to lift heavier fluid from below. A simple example parameterization, used here, is to have a different viscosity

and diffusivity value in the vertical direction than the horizontal, to represent the inhibition of mixing by stratification, and evaluations of different formulations continue as an active area of research (Warner et al. 2005, Fox-Kemper, Ferrari, and Hallberg 2008). We also provide the caveat that operational forecast system resolution continues to increase, and the line between represented dynamics and what must be parameterized continues to move. The parameterized representations must evolve as well.

Given limited computer resources and the need to forecast large areas, most operational ocean forecast systems are based on hydrostatic models. Although nonhydrostatic process can be of importance, in the operational environment, they are represented through parameterization. Therefore, we focus attention on hydrostatic dynamics, which still represent a majority of problems of interest, from here forward.

6. Fundamental solutions of the dynamical equations

The Boussinesq and hydrostatic momentum equations describe a wide range of processes. These should explain some of the basic dynamical relations one may diagnose from operational ocean forecasts. The results from operational ocean predictions have become more realistic over time, and, in doing so, the results become almost as difficult to understand as the ocean. It is important to keep in mind some of the fundamental balances and the assumptions behind them.

One of the most basic is the geostrophic balance obtained by neglecting friction, advection of momentum, and the time rate of change in (10) or, alternatively, assuming a small Rossby number in (22) as well as the ratio R_o/R_e being small. The result is the balance between geostrophic velocity and pressure gradient: $\left(u_g, v_g\right) = \left(-\partial p/\partial y, \partial p/\partial x\right)/f\rho_o$. The subscripts on $\left(u_g, v_g\right)$ indicate that these are the geostrophically balanced part of the total flow. Under what conditions in operational forecasts is the Rossby number small so that the geostrophic balance is reasonable? Consider the situation of a mesoscale eddy, such as those observed generated in the Gulf Stream (Figure 1), with $L = 10^5$ m. The Coriolis parameter f is on the order of 10^{-4} s^{-1}, and u and v are of the order of 0.1 m/s. Under these conditions, $R_o = 0.01$, and so the geostrophic balance is reasonable by (22).

The vertical variation in the geostrophic currents is obtained by taking the z derivative of the geostrophic equation and combining it with the x and y derivatives of the hydrostatic pressure equation. The result is the thermal wind equation

$$\begin{aligned} \frac{\partial u_g}{\partial z} &= \frac{g}{\rho_o f}\frac{\partial \rho}{\partial y} \\ \frac{\partial v_g}{\partial z} &= -\frac{g}{\rho_o f}\frac{\partial \rho}{\partial x} \end{aligned} \tag{27}$$

These fundamental relations are useful for diagnosing observations such as maps of sea surface height observed by satellite altimeter sensors (e.g., Chelton, Schlax, and Samelson 2011) and sea surface temperature as seen from satellite radiometers (e.g., Chavanne and

Klein 2015). The pressure at $z = 0$ (the position of the ocean surface under the conditions of no motion and no forcing) can be approximated as $\rho_o g \eta$, where η is the ocean surface relative to $z = 0$, because the ocean surface varies only by meters and the density variation over this thickness is not a significant factor in computing the pressure. The geostrophic equations immediately provide the surface velocity. From ship transect observations, near surface velocity may be observed by acoustic Doppler current profiler while measuring temperature and salinity to much greater depth (e.g., Callies and Ferrari 2013). The thermal wind equations immediately provide velocity throughout the observed depths (e.g., Pollard and Regier 1992).

An additional simple dynamical relation may be extracted from the equations of motion. In this case, assume the flow is horizontally uniform and R_o/R_e is small in (22). Also, assume there is no pressure gradient. The time rate of change is retained to derive the inertial oscillation, which implies a Rossby number of 1. The resulting balance in the inertial oscillation is $(\partial u/\partial t, \partial v/\partial t) = f\,(v, -u)$. Solutions are $(u, v) = (Re\,(U_o \exp(ift))\,, Im\,(U_o \exp(ift)))$, where the complex constant U_o provides the magnitude and phase of the currents relative to time 0, where *Re* is the real component and *Im* is the imaginary component of a complex value, and where $i = \sqrt{-1}$. The velocity vector traces a circle rotating clockwise through time over one inertial period, which is $2\pi/f$. For a drifter in the ocean under the influence of inertial oscillations, the circle transited over one inertial period has a radius of U_o/f. In this case $L = U_o/f$ and thus $R_o = 1$, as was assumed initially. Such motions are ubiquitous throughout drifter observations. Inertial oscillations are a natural response mode of the ocean to any forcing or change such as sudden forcing by surface winds. In prediction systems outputting results at high frequency, inertial oscillations are a dominant response to sudden changes in wind forcing and create transients lasting for days.

Ekman transport is the steady-state response to wind forcing. Consider first an ocean that is stationary far below the surface, with a specified uniform wind stress, and that is horizontally uniform. Assume in (22) the Rossby number is small, though the ratio R_o/R_e is order 1. Orient the local coordinate system so that the wind stress is in the x coordinate direction and the wind stress magnitude is τ_x. Assume that the vertical diffusivity ν is constant and that the flow is homogeneous horizontally so that the horizontal gradients are zero. The equations of motion reduce to

$$\begin{aligned} fv + \nu \frac{\partial^2 u}{\partial z^2} &= 0 \\ -fu + \nu \frac{\partial^2 v}{\partial z^2} &= 0 \end{aligned} \tag{28}$$

The solution is given by $(u, v) = \tau_x / \left(\rho_o \sqrt{\nu f}\right) \exp\left(L_z z\right) (\cos\left(z/L_z - \pi/4\right), \sin(z/L_z - \pi/4))$ with $L_z = \sqrt{2\nu/f}$ being the Ekman layer depth scale. The currents at the surface are 45° to the right of the wind stress direction, decrease in amplitude with depth, and continually turn clockwise with depth. However, if an eddy viscosity is parameterizing

the effects of Ekman layer turbulence, it tends not to be constant in the vertical, and this solution is not exact. The vertically integrated transport due to a wind stress (τ_x, τ_y) is $(1/(\rho_o f))(\tau_y, -\tau_x)$, a result that is not dependent on the detailed profile of the viscosity. This Ekman transport is 90° to the right of the wind stress in the Northern Hemisphere (90° to the left in the Southern Hemisphere). The effects of Ekman transport near coasts in operational predictions are important. Winds blowing parallel to the coast will create a transport either toward or away from the coast. The result is either a downwelling of warm surface waters or an upwelling of cold deep waters near the coast. The nutrients and cold water brought to the surface in upwelling zones cause dramatic blooms of ocean coastal productivity and foggy coastal weather.

The flow of currents over bathymetry creates a stress on the bottom of the water column, and this generates a bottom Ekman layer. In the case of a bottom Ekman layer, the Ekman transport is 90° to the left of the ocean current direction (in the Northern Hemisphere). As ocean currents flow parallel to coasts along continental shelves, the bottom Ekman layer can move properties on or off the shelf.

In deep water areas, spatial variation in wind stress (τ_x, τ_y) also results in upwelling or downwelling. By the continuity equation (11), and assuming the sea surface position is stationary, the vertical velocity at a depth is the integral from the depth to the surface of the horizontal velocity divergence. If we choose a point a few Ekman layer depth scales below the surface, with small error the vertical velocity is the divergence of the Ekman transport,

$$w_e = (1/\rho_o)\,\nabla \cdot \left(\tau_y/f, -\tau_x/f\right) = (1/\rho_o)\,\mathbf{k}\nabla \times \left(\tau_x/f, \tau_y/f\right) \tag{29}$$

where **k** indicates the vertical component of the curl operator. That is, the vertical velocity at the base of the Ekman layer is determined by the wind stress curl. Later we will examine a simplification of the dynamical equations to quasigeostrophic dynamics, and we will find that these small vertical velocities drive the geostrophically balanced flow.

This vertical velocity due to wind stress curl is a fundamental driver of ocean circulation first elucidated by Sverdrup. The geostrophic equations may be combined to eliminate pressure while retaining the fact that the Coriolis parameter varies with latitude ($f = f_o + \beta y$). Applying continuity to the result yields

$$f_o \frac{\partial w}{\partial z} = v_g \beta \tag{30}$$

Consider the slab of ocean from a level at which velocities are zero to the depth just below the Ekman layer, and assume this slab is uniform in horizontal velocity. By continuity this implies that $\partial v_g/\partial z$ is uniform over depth. If the slab has a thickness H, and the vertical velocity at the top due to the Ekman layer pumping is w_e, then, over the slab, $\partial w/\partial z = w_e/H$. Therefore

$$v_g = (f/\beta)\,(w_e/H) = \nabla \times \left(\tau_x, \tau_y\right) / \left(\rho_o \beta_o H\right) \tag{31}$$

This is the Sverdrup transport, which is the meridional flow driven by the wind stress curl.

The friction velocity $u^* = \sqrt{\tau/\rho_o}$ is often used to scale for near-surface velocities driven by winds. For example, a rough scaling for the depth of the turbulent Ekman layer is u^*/f.

7. Effects of stratification

The density in the momentum equations plays a key part in forcing ocean circulation, and in the previous simplified dynamics the density is provided as a specified field. From the specified density we compute pressure by the hydrostatic balance and compute currents by geostrophy. We want to understand how all these fields interact and evolve over time. Understanding these evolutions from the dynamic point of view lends insight to considerations that are of importance in operational prediction systems. We provide some of the basic dynamical equations that are commonly derived in many texts (Gill 1982, Pedlosky 2013, Cushman-Roisin and Malačič 1997).

Stratification is a basic consideration in ocean predictions, as it strongly controls the evolution and, thus, forecast results. Small vertical density movements in one location lead to horizontal pressure gradients and subsequent response. Examples of the importance of stratification are provided by analytic models of the equatorial current system (McCreary 1981) to fully coupled Earth climate systems (Danabasoglu et al. 2012). Achieving realistic stratification in global models is very difficult, as the forcing is surface momentum, heat fluxes, evaporation, precipitation, and freshwater river fluxes. It is entirely incumbent on the numerical system dynamics to construct proper density structure from only surface forcing (Dunne et al. 2012). First order evaluations of operational global ocean systems are made against observed stratification (Metzger et al. 2014). Higher resolution local prediction systems utilize boundary conditions from global forecasts. Local systems have a much stronger external control on stratification and are not as dependent on the model representation to reconstruct the stratification (Rowley and Mask 2014).

Stratification is a controlling force in the generation of internal waves, which are a response to many types of forcing. One example is the generation as tidal flows oscillate across ridges or sharp topography, such as the shelf break, that is simulated in both global and regional models (Zhang, Fringer, and Ramp 2011, Shriver et al. 2012). Tidal flows across topography generate perturbations of the stratification that propagate as internal waves (referred to as internal tides), and the stratification strength determines the propagation speed. In 12 hours, semidiurnal tides propagate approximately 100 km, a particular fact exploited to observe the ocean surface height expression of the internal tide (Ray and Cartwright 2001). Wave solutions are a natural starting place to understand dynamics, and we begin by considering waves and the effect that stratification has on solutions to the dynamics. Thus, a first step in understanding is to consider the evolution of internal waves,

given the evolution of density. Ignoring diffusive properties in the thermodynamic equations, the density is constant following fluid parcels:

$$\frac{D\rho}{Dt} = \frac{\partial \rho}{\partial t} + u\frac{\partial \rho}{\partial x} + v\frac{\partial \rho}{\partial y} + \frac{\partial \rho}{\partial z} = 0 \tag{32}$$

Begin with the linearized equations of motion from (10), in which all variables are small values. Decompose density as previously in (8). Assume that the pressure p is composed of the hydrostatic pressure $\partial \bar{p}/\partial z = -\bar{\rho}g$ and a deviation p', then, ignoring products between variables that are smaller than the variables themselves, the linearized forms of (10) and (32) are as follows:

$$\begin{aligned}
\frac{\partial u}{\partial t} &= fv - \frac{1}{\rho_o}\frac{\partial p'}{\partial x} \\
\frac{\partial v}{\partial t} &= -fu - \frac{1}{\rho_o}\frac{\partial p'}{\partial y} \\
\rho_o \frac{\partial w}{\partial t} &= -\frac{\partial p'}{\partial z} - \rho' g \\
\frac{\partial \rho'}{\partial t} &+ w\frac{\partial \bar{\rho}}{\partial z} = 0
\end{aligned} \tag{33}$$

Recall from (8) that $\bar{\rho}$ is a function of z only. The horizontal momentum equations in (33) may be decoupled from one another:

$$\begin{aligned}
\left(\frac{\partial^2}{\partial t^2} + f^2\right) u &= -\frac{f}{\rho_o}\frac{\partial p'}{\partial y} - \frac{1}{\rho_o}\frac{\partial^2 p'}{\partial x \partial t} \\
\left(\frac{\partial^2}{\partial t^2} + f^2\right) v &= +\frac{f}{\rho_o}\frac{\partial p'}{\partial x} - \frac{1}{\rho_o}\frac{\partial^2 p'}{\partial y \partial t}
\end{aligned} \tag{34}$$

Horizontal gradients of (34), along with the time derivative of the continuity equation (11), result in elimination of the horizontal velocity:

$$\rho_o \left(\frac{\partial^2}{\partial t^2} + f^2\right) \frac{\partial w}{\partial z} = \left(\frac{\partial^2}{\partial x^2} + \frac{\partial^2}{\partial y^2}\right) \frac{\partial p'}{\partial t} - \frac{\partial f}{\partial y}\frac{\partial p'}{\partial x} \tag{35}$$

For the moment, ignore the influence of Coriolis parameter f, and ignore the influence of the latitudinal dependence of the Coriolis parameter $\partial f/\partial y$. We will return to both these. These equations reduce to provide a governing equation relating vertical velocity and the perturbation pressure (Gill 1982):

$$\frac{\partial^2 w}{\partial t^2} = -\frac{1}{\rho_o}\frac{\partial^2 p'}{\partial t \partial z} - N^2 w \tag{36}$$

where $N = \sqrt{-\frac{g}{\rho_o}\frac{\partial \bar{\rho}}{\partial z}}$ is the Brunt–Väisälä frequency as defined in equation (8). If there is no horizontal flow and the flow has time to adjust to a hydrostatic balance, the perturbation pressure p' is zero. The solution to (36) is a vertical velocity oscillating sinusoidally with frequency N. The Brunt–Väisälä frequency is the rate at which material elements oscillate vertically from an initial displacement in the background density field $\bar{\rho}$. This frequency provides a quantitative measure of the stratification strength.

A single equation may be derived from (33) that provides the evolution of vertical velocity in which the Brunt–Väisälä frequency is a key element:

$$\frac{\partial^2}{\partial t^2}\left(\left(\frac{\partial^2}{\partial x^2}+\frac{\partial^2}{\partial y^2}\right)\rho_o w+\frac{\partial}{\partial z}\rho_o\frac{\partial w}{\partial z}\right)+\left(\frac{\partial^2}{\partial x^2}+\frac{\partial^2}{\partial y^2}\right)\rho_o N^2 w=0 \tag{37}$$

The reduction of horizontal momentum, continuity, and pressure anomalies to a single equation is common, as will be seen in subsequent examination where equations (10) continue to be reduced to illuminate important dynamical relations. What are the unforced waves that satisfy this system? Assume a solution of the form $w = w_A \exp(i\,(kx + ly + mz - \omega t))$ where w_A is a complex number expressing the amplitude and phase relative to time 0, and it is assumed that the solution for w retains only the real part. Substituting into (37), this is a solution if

$$\omega^2 = N^2\frac{k^2+l^2}{k^2+l^2+m^2} \tag{38}$$

The required relation between the frequency ω and wavenumber vector $\mathbf{k} = (k, l, m)$ is the dispersion relation for the system. The wavenumber vector points in a direction perpendicular to the plane of any constant phase within the wave, and the wavelength is $2\pi/|\mathbf{k}|$. Without providing the derivation, if the Coriolis parameter is retained in (12), the dispersion relation is

$$\omega^2 = \frac{N^2\left(k^2+l^2\right)+f^2m^2}{k^2+l^2+m^2} \tag{39}$$

Thus, the internal wave frequency is bounded between f and N. Depending on the latitude, and, thus, the Coriolis parameter, internal tide waves can be within this frequency range, but this is generally a high frequency range that describes other internal waves. Lower frequencies are considered shortly. As the wavenumber vector is rotated toward the horizontal ($k^2 + l^2$ becomes relatively large so that the horizontal wavelength is small relative to the vertical), it can be seen from the dispersion relation (38 and 39) that the frequency approaches N. As the wavenumber vector rotates toward the vertical (so that the horizontal wavelength becomes large relative the vertical), the frequency approaches f.

With a solution for w, the solutions for ρ', p', u and v may be constructed from (35) and (34) assuming that the form is an oscillating exponential $w = w_A \exp(i(kx + ly + mz - \omega t))$ with amplitudes given by

$$\begin{aligned} p'_A &= -w_A \bar{\rho} \omega m \frac{\left(1 - f^2/N^2\right)}{\left(k^2 + l^2 + f^2 m^2/N^2\right)} \\ \rho'_A &= i w_A \bar{\rho} N^2/(g\omega) \\ u_A &= \frac{1}{\bar{\rho}} \frac{\left(k/\omega - ifl/\omega^2\right)}{\left(1 - f^2/\omega^2\right)} p'_A \\ v_A &= \frac{1}{\bar{\rho}} \frac{\left(l/\omega + ifk/\omega^2\right)}{\left(1 - f^2/\omega^2\right)} p'_A \end{aligned} \tag{40}$$

The complex coefficients in (40) vary between the variables and determine the relative phase. Consider planes perpendicular to the wavenumber vector $\mathbf{k} = (k, l, m)$ at the location of maximum vertical displacement of fluid particles (where $w = 0$ and $\partial^2 w/\partial t^2 < 0$), which are the wave crests. Initially assume the Coriolis effects are negligible so that terms with f in (40) are ignored. Pressure anomalies are maximum at the wave crests, and therefore pressure gradients are zero. The position of maximum w is ¼ wavelength in the direction of $\mathbf{k}$ from the crest, where fluid is rising to continue the forward progression. The velocity direction in three dimensions is perpendicular to $\mathbf{k}$, or parallel to the planes of the wave crests. From (39), the highest frequency is N. If forcing is input to the system at higher frequency, it does not propagate as freely propagating internal waves and remains local to the source. Internal wave energy in the ocean is high, with the most apparent being at locations of higher vertical density gradients, such as in the base of the mixed layer or within the thermocline.

Tides are one process generating periodic forcing. Another process is flow moving over periodic bathymetry features that enforce a vertical velocity at the interface. Assume the stratification is constant with buoyancy frequency N. The preceding analysis now considers mean flow. To continue to use the preceding derivation, assume that a bottom topography is moving beneath a stationary ocean. The results may be translated to a coordinate fixed with topography afterward without loss of the conclusions. Also assume a situation in which all variables are constant in the y direction with the sinusoidal topography of amplitude h_b moving in the $-x$ direction as time increases with a speed of U_b:

$$h = h_b \cos(k(x + U_b t)) \tag{41}$$

To continue within the linearized equations (33), the amplitude h_b must be small. Place the vertical origin at the mean vertical position of the topography, and the vertical velocity at $z = 0$ determined by (41) is $w(z = 0) = \partial h/\partial t = -h_b k U_b \sin(k(x + U_b t))$. In order to match the bottom boundary condition for w, the solution to (33) must have a form that is

periodic in x with wavenumber k, and the solution must be periodic in time. The frequency is determined by the translation velocity and wavelength $\omega = kU_b$. The problem is now to determine the vertical wavenumber m to satisfy (38). This leads to the dispersion relation $m^2 = N^2/U_b^2 - k^2$. In this situation, the Froude number is defined by $Fr = U_b k/N$. If $Fr < 1$, the flow speed is less than required to move one topographic wavelength during one period of the Brunt–Väisälä buoyancy period. The solution for m is real, the solution for w is oscillatory, and the direction of m is upward (a result of energy required to propagate away from the bathymetry, which is a level of complexity omitted here). Lines of constant phase tilt toward $-x$ with increasing height as the vertical velocity disturbances propagate upward from the topographic forcing. In the coordinate frame fixed with the bathymetry, the lines of constant phase tilt toward $+x$. If $Fr > 1$, or if the velocity is larger than required to pass one bathymetric wavelength during a buoyancy cycle, the solution for m is imaginary. The vertical velocity is of the form $w = -h_b k U_b \sin(k(x + U_b t)) \exp\left(-\sqrt{k^2 - N^2/U_b^2}\, z\right)$, in which case planes of constant phase are fixed with the topography moving underneath, and the amplitude decreases exponentially with height.

In this situation, the Froude number provides a measure of the importance of the time scale of the stratification relative to the time scale of the forcing acting on the flow. If the Froude number is less than 1, then stratification effects are important. For typical values of the Brunt–Väisälä frequency of 0.01 radians/s, flows of 0.1 m/s, and wavelengths of ~10 km ($k = 6x10^{-4}$ radians/m), $Fr \simeq 0.01$.

An example of the effects of Froude number on the flow over a corrugated topography is provided by MacCready and Pawlak (2001). In this case, rather than just a sinusoidal bathymetry on a flat bottom according to (41), the corrugations are added to a sloping bottom. The Froude number must be less than 1 to generate internal waves, and the sloping bottom imposes a lower bound on the Froude number as well. In Figure 2, the flow over the topography shows strong internal wave generation when the Froude number is larger than the critical value. When currents are reduced below the lower bound, the internal wave generation ends.

Internal wave generation represents a process of energy transfer from one form to another. In the case of tides, energy transforms from the barotropic or external tide into internal tide energy (Egbert and Ray 2000). Around sharp topography, the large-scale flow transforms energy into internal waves and turbulence. These mechanisms typically extract energy from flows resolved by numerical prediction systems into processes that are not resolved, and such processes must be parameterized (Simmons, Hallberg, and Arbic 2004; Jayne and St Laurent 2001; Nikurashin and Ferrari 2010). Even if a numerical system may resolve the energy transfer and subsequent evolution mechanisms, we must consider if predictions are deterministic. In the case of interaction with bottom topography, if bathymetry is well known and a numerical model is sufficiently accurate, a significant portion of the internal wave field may be predictable near the generation region. However, after propagating some distance, the field becomes nondeterministic in that the position of features in the real world do not

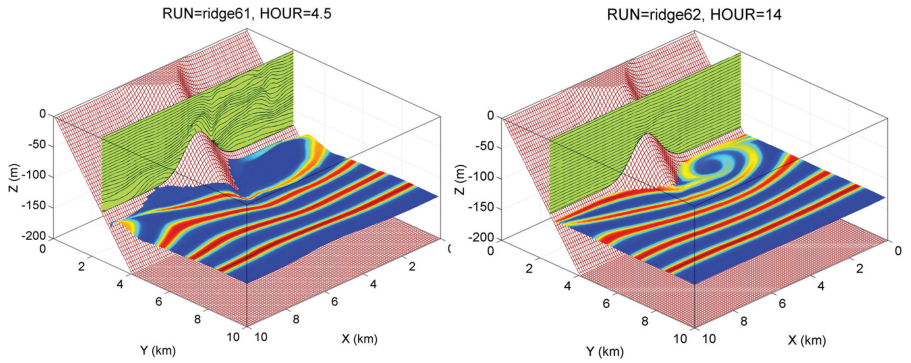

Figure 2. An example of stratified flow over topography on a sloping bottom is provided by MacCready and Pawlak (2001). In both cases the Froude number is less than 1. On the left, internal waves are generated as shown by the model layer interfaces in the green vertical plane. On the right, the velocity is reduced below the lower limit for internal wave generation, and the model interface displacements show minimal perturbations. Image provided courtesy of P MacCready.

match the positions in the model prediction. Such is the case as internal tides propagate through spatially varying stratification that changes propagation speed and eventually leads to significant nonstationary energy (Ray and Zaron 2011).

8. Vertical modes

The previous section began with the assumption of a constant Brunt–Väisälä frequency over the water column. This may be a reasonable approximation in local situations; however, it is typically not. The stratification strength changes significantly over depth, and this affects how energy is distributed vertically. Accurate ocean predictions must begin with accurate stratification.

In addition, the previous section provided examples of variability mainly at high frequencies. Insight to dynamics at larger scales can be provided by accounting for vertical structure in the Brunt–Väisälä frequency, which leads to the concept of vertical modes. The first step is to show that the ocean may be treated as a superposition of solutions that are all similar in the horizontal with different vertical structure. This allows us to understand the common horizontal variations for any vertical mode. The implication of large horizontal scales can be discerned from the relation between pressure and density using the solutions in (40)

$$\frac{\partial p'}{\partial z} = -g\frac{1 - f^2/N^2}{1 + \left(k^2 + l^2\right)/m^2}\rho' \tag{42}$$

as $\left(k^2 + l^2\right)/m^2 \to 0$ and as $f < N$, the hydrostatic balance returns. A scaling analysis of terms in (33) under the assumption that horizontal lengths are much greater than vertical also reaches the same result.

In this case, the governing equation equivalent to (37) for w becomes

$$\frac{\partial^2}{\partial t^2}\left(\frac{\partial}{\partial z}\bar{\rho}\frac{\partial w}{\partial z}\right)+\left(\frac{\partial^2}{\partial x^2}+\frac{\partial^2}{\partial y^2}\right)\bar{\rho}N^2 w=0 \tag{43}$$

If $\bar{\rho}$ varies over vertical scales much larger than w, the dispersion relation is $\omega^2 = N^2\left(k^2+l^2\right)/m^2$. However, the intent is to examine larger scales on the order of $m=\pi/H$, where H is the total water depth. Because we are considering scales of the entire water column, w and $\bar{\rho}$ can vary over equal distances. Therefore, we must pursue a different solution by returning to (35) and (36). Equation (35) remains unaltered, and, if we assume hydrostatic balance in the long horizontal scale limit, the term $\partial^2 w/\partial t^2$ in (36) becomes zero. A method widely used in fluid dynamics is the separation of variables, in which the pressure and vertical velocity are separated into the product of two functions each. One is a function only of z and the other a function of only (x, y, t)

$$\begin{aligned} p' &= p_v(z)\, p_h(x, y, t) \\ w' &= w_v(z)\, w_h(x, y, t) \end{aligned} \tag{44}$$

where the subscripts denote vertical and horizontal functions. We must retain the vertical variation in density as appropriate in the equations (35) and (36), and we use the mean vertical density structure represented by $\bar{\rho}(z)$. Using these forms in (35) and (36), the four resulting equations provide the solutions for the vertical and horizontal components:

$$\frac{1}{\rho_o}p_v = C^2\frac{\partial w_v}{\partial z} \tag{45}$$

$$\frac{1}{\rho_o}\frac{\partial p_v}{\partial z} = -N^2 w_v \tag{46}$$

$$\left(\frac{\partial^2}{\partial t^2}+f^2\right)w_h = C^2\left(\left(\frac{\partial^2}{\partial x^2}+\frac{\partial^2}{\partial y^2}\right)\frac{\partial}{\partial t}-\frac{\partial f}{\partial y}\frac{\partial}{\partial x}\right)p_h \tag{47}$$

$$w_h = \frac{\partial p_h}{\partial t} \tag{48}$$

where the Coriolis parameter terms are retained in the horizontal equations. The vertical equations (45, 46) can be reduced to a single variable that results in the Sturm–Louisville problem for either the vertical structure w_v or p_v:

$$\begin{aligned} \frac{\partial}{\partial z}\bar{\rho}\frac{\partial w_v}{\partial z} &= -\frac{1}{C^2}\rho_o N^2 w_v \\ \frac{\partial}{\partial z}\frac{1}{\bar{\rho}N^2}\frac{\partial p_v}{\partial z} &= -\frac{1}{C^2}\frac{1}{\bar{\rho}}p_v \end{aligned} \tag{49}$$

For an observed density profile $\bar{\rho}$ and corresponding Brunt–Väisälä frequency N, multiple solutions to (49) are possible with discrete and decreasing values of C^2 identified as C_n^2.

If the separation of variables for u and v is conducted similarly to p', it is apparent that the vertical structure of the horizontal velocity field is the same as p'. According to the theory of the Sturm– Louisville problem, the n^{th} mode contains n zero crossings or reversals in current direction. The 0^{th} mode has unidirectional currents throughout the water column, and the 1^{st} mode has one zero crossing in currents so that surface and deep currents are oppositely directed.

Ignoring the Coriolis parameter terms in the horizontal equations (47), these are the same as the equations governing the development of a thin fluid with uniform properties over depth and a propagation speed of C. Thus, the ocean can be treated as a superposition of modes with vertical structure provided by the solutions to (49) corresponding to C_n, and the horizontal dynamics associated with each are very similar. The main difference is the underlying speed at which waves propagate according to solutions to (49). An example of the vertical structure is provided in Figure 3. Two observed profiles of temperature and salinity are used. One is north of the Gulf Stream and one is south in order to highlight the difference in stratification and its effects. The Brunt–Väisälä frequency is computed from each profile, and the associated modes are provided for w and p', which is the same as the vertical structure for (u, v). The profile north of the Gulf Stream has higher stratification in the range of 100–500 m depth, whereas the profile south of the Gulf Stream has weaker stratification over the deeper range 500–1000 m depth. This changes the depth of pressure and velocity variability between the areas north and south of the Gulf Stream.

In a thin fluid with uniform properties over depth H, the propagation speed is the barotropic wave speed $\sqrt{gH}$. The propagation speeds in a stratified fluid are much less. One example is made by representing the ocean as a two layer fluid with less dense water over more dense water and the assumption that the lower layer is infinitely deep with no velocity. This is a very simple representation of the thermocline variability and is referred to as a reduced gravity model. Waves that are a result of the interface displacement between the upper and lower layer propagate at a speed of $\sqrt{g' H_u}$ where H_u is the thickness of the upper layer at rest and the reduced gravity is defined as $g' = g\left(\rho_u - \rho_l\right)/\rho_l$. This typically has a very small value as the density difference between the upper and lower layers $(\rho_u - \rho_l)$ is much smaller than the lower layer density ρ_l. Thus, typically, $C_n << C_0$ for $n > 0$. An example in the next section based on observations of propagating waves indicates a typical value of $g' = 0.001$.

Reduced gravity models are very efficient to run but the represented processes are restricted. Therefore, these systems useful for long experiments when particular processes are of interest (Qiu and Chen 2012). For operational applications, the range of ocean processes that must be represented is much larger than what a reduced gravity model may represent. A much more complex model should still retain the ability to forecast reduced gravity physics, and thus it is useful to understand these dynamics when diagnosing a complex system.

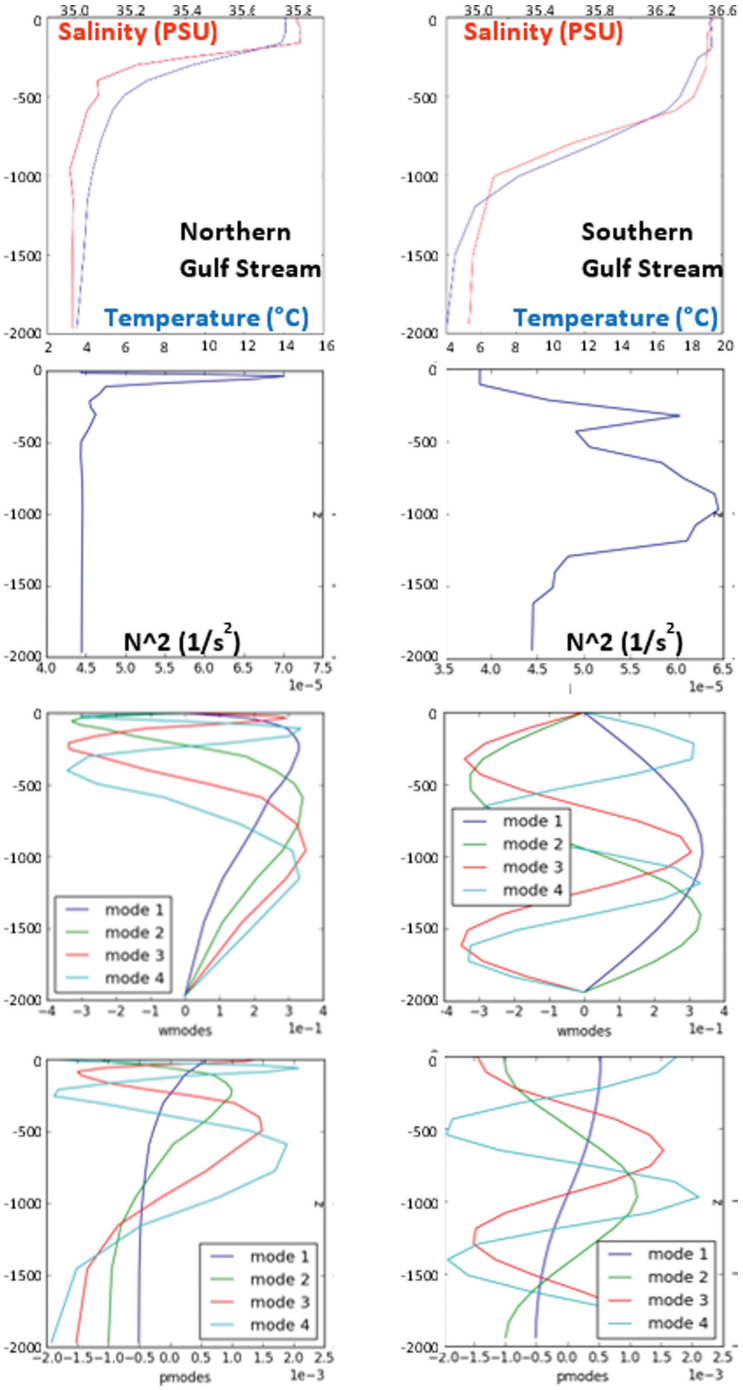

Figure 3. Vertical modes north (68.05W, 39.00N, left column) and south (67.83W, 34.15N, right column) of the Gulf Stream. The top row is the observed temperature and salinity, and the corresponding Brunt–Väisälä frequency is the second row. The computed vertical models of w are shown in the third row, and the modes of p' are the bottom row. Image provided courtesy of B Linzell.

The terms in (47) related to the Coriolis parameter and its variation with latitude lead to interestingly different solutions from the usual shallow water wave solutions. We now turn attention to these terms and their influence on the large scale horizontal dynamics.

9. Large scale horizontal waves

Observation of ocean features such as the Gulf Stream and mesoscale eddies in Figure 1 show that spatial scales are large and time scales are longer than the planet rotation period. These scales are the primary targets for most global to regional forecast systems (Tonani et al. 2015). Forecasts of these scales provide information for problems such as disasters (Tsumune et al. 2012) and for planning marine operations (Smith et al. 2010).

Building on the concept that the ocean variations can be decomposed into vertical modes, and that each mode has similar horizontal dynamics differentiated by propagation speed, we now examine dynamics relevant for large scale waves. Again, large scale implies that the horizontal scales are much larger than the vertical so that the hydrostatic balance is appropriate (42). First, we examine unforced wave solutions to the linearized equations (33) and initially ignore the latitudinal variation in Coriolis parameter. In which case, (47) leads to the equation governing the horizontal pressure field

$$\left(\frac{\partial^2}{\partial t^2} + f^2\right) p_h = C_n^2 \left(\frac{\partial^2}{\partial x^2} + \frac{\partial^2}{\partial y^2}\right) p_h \tag{50}$$

where the speed C_n is dependent on the particular vertical mode being considered. We seek solutions of the form $p_h = p_{hA} \exp(i\,(kx + ly - \omega t))$, and this is a solution of equation (50) if

$$\omega^2 = f^2 + C_n^2 \left(k^2 + l^2\right) \tag{51}$$

Note the similarity to (39), assuming the long wave limit $\left(k^2 + l^2\right)/m^2 \to 0$, in which case the phase speed of (39), N^2/m^2, is replaced by C_n^2. The velocity field provided in the form $(u_h, v_h) = (u_{hA}, v_{hA}) \exp(i\,(kx + ly - \omega t))$ from (34) is then

$$\begin{aligned} u_{hA} &= \frac{1}{\rho_o} \frac{-k\omega - ifl}{\omega^2 - f^2} p_{hA} \\ v_{hA} &= \frac{1}{\rho_o} \frac{l\omega + ifk}{\omega^2 - f^2} p_{hA} \end{aligned} \tag{52}$$

These solutions are Poincare waves. The dispersion relation (51) indicates that the frequency is always greater than f, and, according to (52), the velocity field is not in geostrophic balance.

The unforced solutions to the linearized equations of motion (33) indicate the natural ocean dynamical means to respond to an input forcing. One example of semidiurnal Poincare waves in response to external forcing is provided in the Santa Cruz basin using

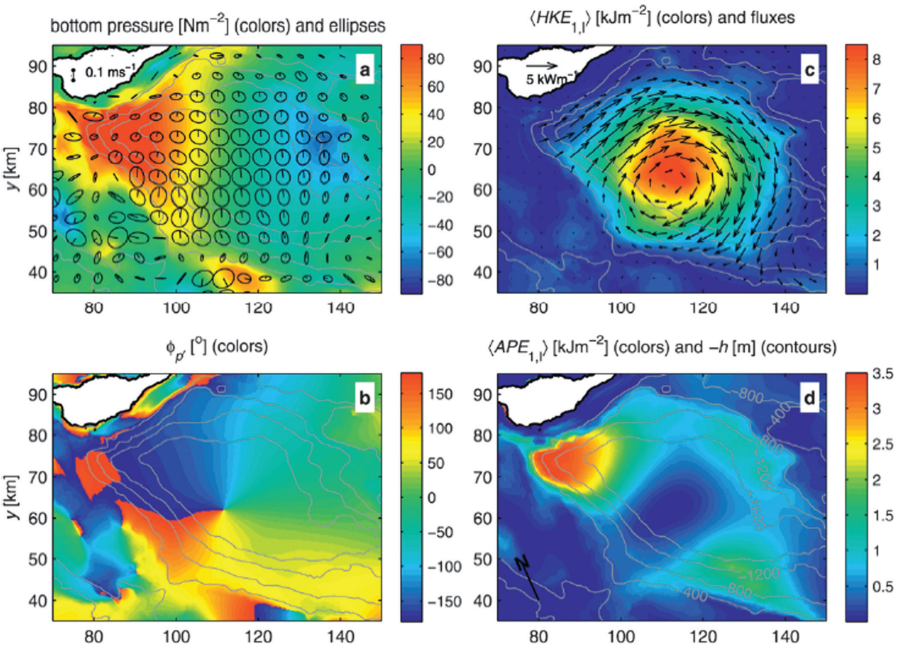

Figure 4. An example of a Poincare wave generated in a realistic geometry through forcing within an enclosed basin provided. (a) Pressure, (b) phase of pressure, (c) horizontal kinetic energy and energy flux vectors, (d) potential energy due to buoyancy displacement. Image provided courtesy of M Buijsman.

the ROMS model (Figure 4; Buijsman et al. 2012). In this case, regular tidal current forcing inputs energy to a local enclosed small-scale basin. The response is a vertical and horizontal first-mode wave that is progressive along the azimuthal direction and standing along the radial axis of the enclosed basin. The pressure field within the model experiment indicates consistency with phase increasing in a clockwise direction. The implication is that the Poincare wave and its energy flux propagates clockwise within the basin. The largest potential energy due to displacements of buoyancy surfaces occurs on the outer edge of the domain with a minimum potential energy variation in the domain center. Kinetic energy has the largest magnitudes in the domain center.

The Kelvin wave is another large-scale solution to the linearized dynamical equations (33) when bounded on one side. Consider the situation where a solid vertical wall exists at $y = 0$, vertical and horizontal solutions are separated so that (50) describes the horizontal evolution, and the horizontal solution is expressed as $p_h = p_{hy}(y) \exp(i(kx - \omega t))$. Then the horizontal dynamics from (50) provide

$$\frac{\partial^2 p_{hy}}{\partial y^2} + \left(\frac{1}{C_n^2} \left(\omega^2 - f^2 \right) - k^2 \right) p_{hy} = 0 \tag{53}$$

The boundary condition for $v\,(y = 0) = 0$ when used with (34) implies

$$\left(fk + \omega\frac{\partial}{\partial y}\right) p_{hy}\Big|_{y=0} = 0 \tag{54}$$

First note that Poincare waves still are solutions to the bounded problem described by equations (53) and (54). If $p_{hy} = \mathrm{Re}\left(ip_{hyA}\exp(ily)\right)$ where p_{hyA} is a real valued amplitude, the solution satisfies the boundary condition (54) and the dynamical relation (53) if $\omega^2 = C_n^2\left(k^2 + l^2\right) + f^2$, which is the dispersion relation for Poincare waves given in (51). The main change from Poincare waves in a laterally unbounded medium is that the phase is determined by the boundary condition. This situation is highlighted in Figure 4 as the Poincare wave propagates around the edges of the basin. The boundary condition also enables the Kelvin wave.

In an infinite horizontal domain, solutions growing exponentially are not allowed as amplitude becomes unrealistically unbounded. With a lateral boundary, the unbounded portion of the solution may be suppressed. Specify $p_{hy} = p_{hyA}\exp(\mp ly)$ with convention that the upper sign (negative in this case) applies for $y > 0$ and the lower sign (positive) applies for $y < 0$. The result is that the solution decreases in amplitude with distance from $y = 0$. With this horizontal form, the dynamical relation (53) produces $\omega^2 = C_n^2\left(k^2 - l^2\right) + f^2$, and the boundary condition (54) results in $(fk \pm \omega l)|_{y=0} = 0$. The boundary condition implies $\omega = \mp fk/l$. In the Northern Hemisphere, if the wall is not on the equator, then waves north of the wall propagate to the east and waves south of the wall propagate to the west regardless of the sign of k. These are Kelvin waves. An interesting situation exists on the equator where Coriolis changes sign on opposite sides of the wall so that the waves on both sides of a wall on the equator propagate to the east. From the perspective of the wave, in the Northern Hemisphere the boundary is on the right-hand side when facing in the direction of propagation and on the left-hand side in the Southern Hemisphere.

Kelvin and Poincare waves play a critical role in the propagation of tides. The moon and sun cause the tides by gravitational attraction. A simple, static tidal forcing response suggests that high tides occur on the near side of the earth toward a gravitationally attracting body, and high tides also occur on the far side of the earth due to the decreased gravitational attraction and increased centrifugal force as the earth and other body orbit the center of mass of the two. However, the sun and moon are not statically located, so the tidal bulges must propagate to keep up. The tidal bulge cannot propagate freely as the Earth rotates underneath because of the interaction with land boundaries. These waves are the primary mechanism by which the basin scale propagation of tides occurs, and much of the science of tides and tidal prediction is involved in studying these waves.

With the dynamical relation and boundary condition, it is possible to show l must satisfy

$$R_n = 1/l = C_n/f \tag{55}$$

R_n is the Rossby radius of deformation, and it is different for each vertical mode corresponding to C_n. A global examination of the first mode Rossby radius is provided by

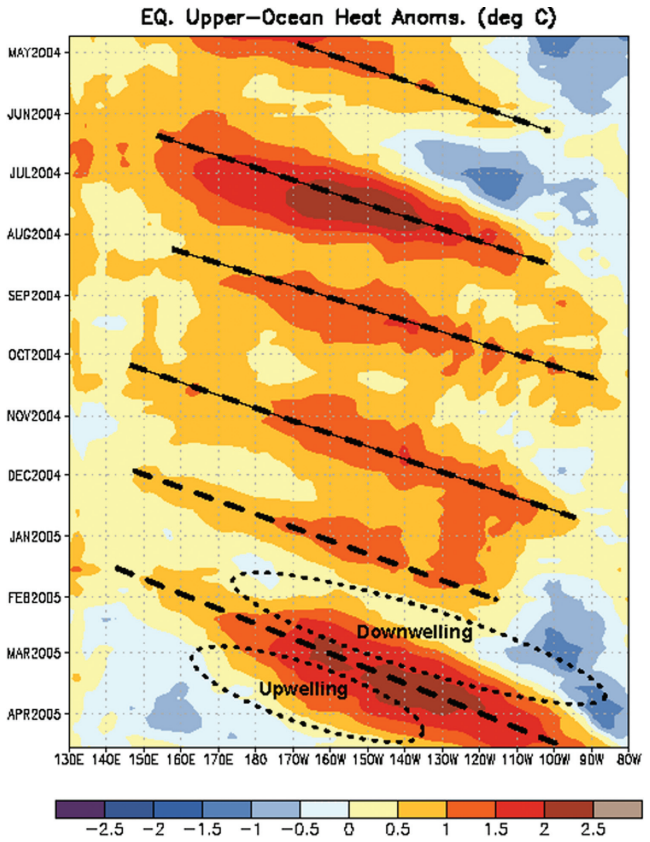

Figure 5. An example of Kelvin wave propagation along the equatorial Pacific from May through April 2004. The Tropical Atmosphere Ocean (TAO) data analysis shows the upper 300 m heat content as anomalies from the 1992–2003 mean. As the Kelvin waves propagate, the thermocline moves vertically. The upper ocean total heat content changes as a result. The downward thermocline movement at the wave front is referred to as downwelling, and the upward thermocline movement in the wave lee is referred to as upwelling. From the 5 May 2005 Climate Prediction Center El Niño–Southern Oscillation (ENSO) diagnostic discussion.

Chelton et al. (1998). It is the distance an unforced wave propagates during one pendulum day. With the definition (55), the dispersion relation becomes $\omega^2 = C_n^2 k^2$. With the relation $\omega = \pm fk/l$ determined by the boundary condition, according to (34), $v = 0$ everywhere. The geostrophic balance is then satisfied by u according to (33). Also notice that the frequency can be much less than f if $k \ll l$, that is, according to (55) if the wavelength in the direction along the wall is greater than the Rossby radius of deformation.

Observations of Kelvin wave propagation are shown in Figure 5. Note the propagation speed to the east is approximately 2 m/s. This is far less than the zero-mode propagation

speed of $\sqrt{gH} = 200$ m/s using $H = 4000$ m. For 2 m/s propagation, the reduced gravity $g' = 0.001$.

Wave solutions in the simplified dynamics are natural responses to changes in ocean forcing, and Kelvin waves are a response during the El-Niño process. Typically, winds from the east blow across the tropical Pacific Ocean. Because of Ekman transport and the change in sign of Coriolis across the equator, a divergence and associated upwelling occurs along the equator that brings cooler waters to the surface. A steady-state balance is established, and when the winds weaken the system must produce a transient response. The response is in the form of a pair of Kelvin waves propagating from west to east on opposite sides of the equator (Kug et al. 2010). The two waves balance one another across the equator. This creates the equivalent of a no-flow boundary along the equator for each wave. As the waves propagate toward the east, the stratification changes, and warm water appears on the ocean surface as the Kelvin waves pass. The Kelvin wave pressure field results in a high sea surface height that propagates to the east with the waves. These are observed as shown in Figure 5.

Upon reaching the eastern Pacific boundary, the Kelvin wave continues propagation both northward and southward along the American continents with the coastlines serving as a solid wall to support them (Hermann et al. 2009). The associated temperature and salinity fluctuations impact fisheries (Williams and Terawasi 2011). Predicting the El-Niño onset effects requires accurately representing the propagation of Kelvin waves, which in turn requires the accurate representation of vertical stratification distribution.

10. Rossby wave dynamics

So far, the Kelvin wave is one solution that has a frequency much less than f at large spatial scales. As Kelvin waves propagate poleward along the American continents during the El-Niño process, perturbations remain in their wake. The ocean response to these perturbations is provided by Rossby waves (Fu and Qiu 2002; White 1985). The dynamics are due to one term in equation (35) that has yet to be addressed, which is $\partial f/\partial y \; \partial p'/\partial x$. Assume the latitudinal variation of the Coriolis parameter is locally linear, as in equation (21). The term in equation (35) involving the gradient of Coriolis becomes $\beta \partial p'/\partial x$. If the flow is geostrophic, this term can be recognized as being proportional to βv_g, and the question becomes, how does the meridional velocity interaction with Coriolis variation affect ocean dynamics? It should also be noted that the Sverdrup balance (30) contains this term.

We must explicitly bring out the larger scale and lower frequency variations in (33). From many observations in the ocean, the geostrophic balance holds with high accuracy. However, the geostrophic balance does not indicate how the flow evolves. It simply diagnoses the velocity from the pressure. Deviations from geostrophy interact to create a time evolving flow field. Thus, we seek solutions that possess several properties: 1) the flow field contains small deviations from geostrophy, 2) horizontal scales are large on the order of 100 km,

and 3) time periods are long relative to $1/f$. The result will be the equations that are not geostrophic but quasigeostrophic.

These considerations select a subset of the time and space scale domain as well as the relative importance of variable relations within the dynamical equations. We can exploit the nondimensional dynamical equations (22–25) along with the nondimensional constants of the Rossby, Froude, and Reynolds numbers. Consider length scales of 10^5 m, time scales of 10^6 s, midlatitudes so that $f = 10^{-4}\text{s}^{-1}$, water depths of 10^3 m, and a stratification with $N = 10^{-2}$ s^{-1}, the nondimensional parameters result in $R_o = 10^{-2}$, $Fr = 10^{-2}$, $\beta = 10^{-2}$, and assume R_o/R_e is smaller than 10^{-2} so that frictional processes are ignored.

The following analysis would certainly change if the choices for scales did not produce nondimensional parameters that were so conveniently the same. Fortuitously, this allows an expansion of each variable in a power series of a parameter such as $u = u_0 + \varepsilon u_1 + \varepsilon^2 u_2 + \ldots$, where the parameter ε is a small number such as 10^{-2} and each u_i is order 1. The numerical subscripts on the variables indicate the order of the small parameter multiplying them. These choices allow all the nondimensional parameters in (22–25) to be replaced by ε. When substituting the power expansion in for each variable, it allows variables of like powers in ε to balance one another. For example, the horizontal momentum equations of (22–25) provide a balance in zero-order terms of in ε of $(u_0, v_0) = (-\partial p_0/\partial y, \partial p_0/\partial x)$ (subscripts note the order ε). When redimensionalized, this is the geostrophic balance, which is a result of the assumed scales. With the definition of $\nabla_H \pi_0 = -\mathbf{k} \times \mathbf{V}_{H0}$, by continuity of (25), $\partial w_0/\partial z = 0$. Over a flat bottom where $w = 0$ the implication is that w_0 is 0 throughout the water column. The vertical momentum equation (23) in the 0 order balance leads to the hydrostatic relation. Finally, the evolution of buoyancy or density (24) leads to the time rate of change of ρ_0' is 0. The 0 order balance of the equations of motion leads to the usual situation in which a specified pressure field allows diagnosis of geostrophic velocity, though there is no time evolution.

Now we can examine the balances involved in the terms related to the first order ε. The order 1 balance remains hydrostatic and nondivergent, and also results in

$$R_o \left(\frac{\partial V_{H0}}{\partial t} + V_{H0} \cdot \nabla V_{H0} \right) + \nabla_H \pi_1 + \mathbf{k} \times \mathbf{V}_{H1} + \frac{\beta y}{f_o} \mathbf{k} \times \mathbf{V}_{H0} = 0 \tag{56}$$

$$\frac{\partial b_1}{\partial t} + \mathbf{V}_{H0} \cdot \nabla b_1 + w_1 \frac{N^2}{N_o^2} = 0 \tag{57}$$

The order 1 horizontal momentum equations (56) are combined by continuity. Given that the 0 order flow is geostrophically balanced, the 0 order velocities in (56) are replaced by gradients of the 0 order pressure field.

$$\left(R_o \left(\frac{\partial}{\partial t} - \frac{\partial \pi_0'}{\partial y} \frac{\partial}{\partial x} + \frac{\partial \pi_0'}{\partial x} \frac{\partial}{\partial y} \right) \left(\frac{\partial^2}{\partial y^2} + \frac{\partial^2}{\partial x^2} \right) + \beta \frac{\partial}{\partial x} \right) \pi_0' = -\frac{\partial w_1}{\partial z} \tag{58}$$

Similarly, the hydrostatic relation and the buoyancy evolution (57) result in

$$\frac{\partial w_1}{\partial z} = \left(\frac{\partial}{\partial t} - \frac{\partial \pi_0'}{\partial y}\frac{\partial}{\partial x} + \frac{\partial \pi_0'}{\partial x}\frac{\partial}{\partial y}\right)\left(\frac{\partial}{\partial z}\left(\frac{1}{N^2}\frac{\partial \pi_0'}{\partial z}\right)\right) \tag{59}$$

Equations (58) and (59) are the quasigeostrophic counterparts to the results from the linear equations (35) and (36). Note the vertical velocity gradient driving the 0 order pressure π_0' in (58). It was noted earlier that wind stress curl drives the vertical velocity at the base of the Ekman layer (29). The order one vertical velocity gradient on the right-hand side of (58) drives the zero-order pressure evolution of π_0'. The combination of (58) and (59) then provides the equation for the evolution of π_0' that applies to large-scale, long-time-period geostrophic flows. The governing equation is redimensionalized, and the results expressed in terms of the 0 order pressure field p_0'.

$$\left(\left(\frac{\partial}{\partial t} - \frac{1}{\rho_o f_o}\frac{\partial p_0'}{\partial y}\frac{\partial}{\partial x} + \frac{1}{\rho_o f_o}\frac{\partial p_0'}{\partial x}\frac{\partial}{\partial x}\right)\left(\frac{\partial^2}{\partial x^2} + \frac{\partial^2}{\partial y^2} + \frac{\partial}{\partial z}\left(\frac{f_o^2}{N^2}\frac{\partial}{\partial z}\right)\right) + \beta\frac{\partial}{\partial x}\right) p_0' = 0 \tag{60}$$

Because the zero-order balance is geostrophic, horizontal pressure gradients can be interpreted as the geostrophic flow $\left(u_g\frac{\partial}{\partial x}, v_g\frac{\partial}{\partial x}\right) = 1/\rho_o f_o\left(-\frac{\partial p_0'}{\partial y}\frac{\partial}{\partial x}, \frac{\partial p_0'}{\partial x}\frac{\partial}{\partial x}\right)$. The first set of operators in (60) is the total derivative with advection by geostrophic velocity rather than the total velocity. The second set of operators includes $\left(\partial^2/\partial x^2 + \partial^2/\partial y^2\right) p_0'$, which is proportional to the vorticity of the geostrophic flow. The term $\beta\partial/\partial x$ is proportional to the meridional velocity times the latitudinal variation in Coriolis. When ignoring the vertical variability (assuming constant N), (60) states a conservation of vorticity and βv_g. As vorticity increases, βv_g must decrease and vice versa. Thus, an initial perturbation in vorticity has a restoring force by meridional movement changing the latitude and changing the local Coriolis parameter. Obviously, wave solutions should be examined. Assuming small amplitude values of all variables, the advective terms are not significant. We are seeking solutions of the form $p_0' = p_{0A}' \exp\left(i\left(kx + ly + mz - \omega t\right)\right)$. This form with (60) leads to the dispersion relation

$$\omega = \frac{-\beta_o k}{l^2 + k^2 + \frac{f_o^2}{N^2}m^2} \tag{61}$$

This results in a unique character. Regardless of the sign of the eastward wavenumber k, the phase propagation direction is westward. These waves are natural mode of the ocean that are initiated in response to changes in forcing.

Kelvin waves and Rossby waves play a joint role in the El-Niño process. As the Kelvin waves reach the American continents, the high sea surface height builds along the continents and begins to propagate to the north and south. The pressure anomaly along the American continental coasts results in the generation of Rossby waves that propagate to the west.

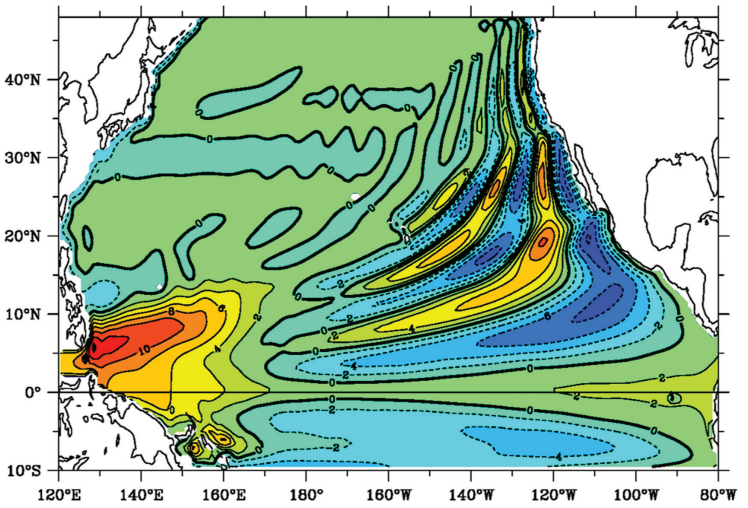

Figure 6. An example of Rossby wave propagation generated by equatorial wind variations shows the response to Kelvin waves in the form of Rossby waves propagating westward from the American continental coasts. The waves refract toward the poles due to changes in phase speed with latitude. Image provided courtesy of B Qiu.

Figure 6 from Qiu, Miao, and Müller (1997) provides an example from a reduced gravity numerical model. The equatorial wind forcing is an analytical seasonal zonal forcing that results in annually generated Rossby waves. The Rossby wave propagation speed at lower latitudes is faster than at high latitudes because of latitudinal variations in f. The waves refract toward the poles over time. Spatial stratification changes are not represented in the model result of Figure 6, though these do add to the latitudinal changes in propagation speed. At higher latitudes the time to cross the Pacific Ocean can be many years. The response times are very important because they indicate the time over which the ocean adjusts to perturbations. Determining if an ocean model is correctly representing dynamical processes can require integration over several times the system response period to allow initial condition transients to damp out and to produce the evolving response to events.

Predictions of El-Niño influence decisions on time scales of months as preparations are made in fisheries and agriculture for expected changing conditions. There is forecast skill at this time scale, and the predictive capability for these problems has continued to improve over time (Barnston et al. 2012).

Rossby waves are closely related with their more nonlinear cousins: mesoscale eddies. In fact, a famous paper featuring the first satellite observations of "Rossby waves" (Chelton et al. 1998) caused quite a stir when the waves did everything right, except propagate at the right speed. Theories to explain why multiplied, but, in the end, revisiting the problem with better data from multiple, simultaneous satellite perspectives revealed that these were not waves at all, but eddies (Chelton, Schlax, and Samelson 2011). Since eddies are dynamically

similar to Rossby waves, they shared the westward propagation and length and time scales, but their nonlinearity slows their propagation relative to the linear wave solutions. Both Rossby waves and mesoscale eddies can be formed by baroclinic instability, the topic of the next section.

11. Mesoscale eddies

Returning to Figure 1, the Gulf Stream flow is part of the large-scale gyre circulation, and mesoscale eddies are generated by meanders in the stream. Eddies, such as those with 300 km scales in Figure 1, have significant impact on many ocean applications. The mesoscale features associated with the Gulf Stream are not unique. Such processes are observed throughout the oceans including within the interior of the large-scale gyres. Eddies have been the focus of ocean forecasts on predictive scales of 3 to 30 days. The dynamics involved in mesoscale eddy evaluation are nonlinear (Early, Samelson, and Chelton 2011). Thus, it is not possible to analytically provide solutions over long time periods. However, we can understand the initiation process, determine the nonlinear growth rate, and estimate expected length scales.

By the geostrophic balance, pressure is higher on the south side of the Gulf Stream. Observations show deep currents are weaker, and the thermal wind equation (27) indicates there are vertical gradients of density associated with the Gulf Stream flow. On the south side of the Gulf Stream, warm light waters exist in the upper ocean that are adjacent to the cold heavy waters on the north side, and this is reflected by the in situ profiles of Figure 3. The sea surface height on the south side is also higher than on the north side (Niiler, Maximenko, and McWilliams 2003). This provides a canonical situation of an eastward current in which pressure drives geostrophic flow that weakens over depth. Now we can examine how perturbations about this current develop over time. The result is that under the right circumstances, perturbations grow over time. The perturbations lead to north and south meandering of the Gulf Stream that grow. The perturbations eventually lead to isolated rings pinching off. Thus, there is a fundamental mechanism by which the large scale circulation generates smaller scale features. The mesoscale eddy field is fundamental as it drives significant variations in density and thus temperature and salinity, which in turn leads to variation in biological properties and interactions with the atmosphere.

The energy driving mesoscale eddies is from the large scale circulation. Potential energy is stored in the Gulf Stream in the form of vertical displacement of pressure surfaces. The ocean mesoscale eddy generation is a mechanism that converts the available potential energy into kinetic energy in the eddy field. The theory was initially developed by Eady (1949) and additional dynamics were included by Charney (1947). Further observations and analyses were extensively provided by the MODE Group and others (MODE Group 1978, Richman, Wunsch, and Hogg 1977, Robinson and McWilliams 1974, Smith 2007, Spall 2000).

Begin by defining the flow of a canonical Gulf Stream containing a uniform surface velocity U_0 in the x direction that is geostrophically balanced, and speed decreases with

depth to form a vertical shear $U = U_0\,(1 + z/H)$. The surface flow U_0 requires a pressure gradient by the geostrophic balance, and the pressure at the surface is provided by the sea surface height so that $\eta = -U_0 g y/f_o$. At depth, the pressure field according to the geostrophic balance is

$$p'\,(x, y, z) = -f_o \rho_o U_0 y\,(1 + z/H) \tag{62}$$

By the hydrostatic relation, the density field is $\rho'\,(x, y, z) = f_o \rho_o U_0 y/gH$. There is initially no variation of the field in the x direction. At a given depth, waters south of $y = 0$ are lower density (warmer) and waters to the north are higher density (colder) in agreement with in situ observations of Figure 3. The analysis is restricted to examining small departures from the mean field in equation (62). These processes are long time period, large-scale, have small deviations from geostrophy, and are small deviations from the Gulf Stream flow. Therefore, quasigeostrophic dynamics (60) are appropriate. In the simple examination provided here, the effects of β are not considered, and stratification measured by the Brunt–Väisälä frequency N is assumed to be a constant value. The total state is a contribution of three parts. Pressure is composed of the mean variation over depth of $\bar{p}\,(z)$, the canonical Gulf Stream p' from equation (62), and the perturbations to the Gulf Stream flow p''. Since we are searching for perturbations that initially grow, we can assume that the perturbations about the Gulf Stream flow are small, and the dynamics are linearized around the background state (62). Under these considerations the quasigeostrophic governing equation from equation (60) is then

$$\left(\frac{\partial}{\partial t} + (U_0\,(1 + z/H))\,\frac{\partial}{\partial x}\right)\left(\frac{\partial^2}{\partial x^2} + \frac{\partial^2}{\partial y^2} + \frac{f_o^2}{N^2}\frac{\partial^2}{\partial z^2}\right) p'' = 0 \tag{63}$$

The equation indicates that wave solutions are appropriate in the y direction, propagating waves are appropriate in the x direction, and a separate solution must be constructed in the vertical z direction. Thus, solutions can be sought of the form $p'' = p''_V\,(z) \exp\,(i\,(kx + ly - \omega t))$. Solutions that grow in time have a value of ω that is imaginary and positive.

Although we are assuming an infinite and uniform horizontal domain, the vertical structure of p''_V must satisfy the upper and lower boundary conditions. Assuming a simple flat bottom ocean, at the bottom and surface the boundary condition is $w = 0$. The solutions are composed of hyperbolic sines and cosines in the vertical of the form $p''_V\,(z) = a \sinh\,(cz) + b \cosh\,(cz)$ where $c^2 = \left(k^2 + l^2\right) N^2/f_o^2$. The relative amplitudes a and b are determined from the vertical boundary condition, and a second condition is derived for which the frequency is an imaginary number. This occurs when

$$\frac{1}{4} H^2 c^2 - Hc \coth\,(Hc) + 1 < 0 \tag{64}$$

When $Hc < 2.4$, the flow is unstable and perturbations grow in time. The wavelength that leads to the most unstable perturbation or the fastest growing perturbation will dominate

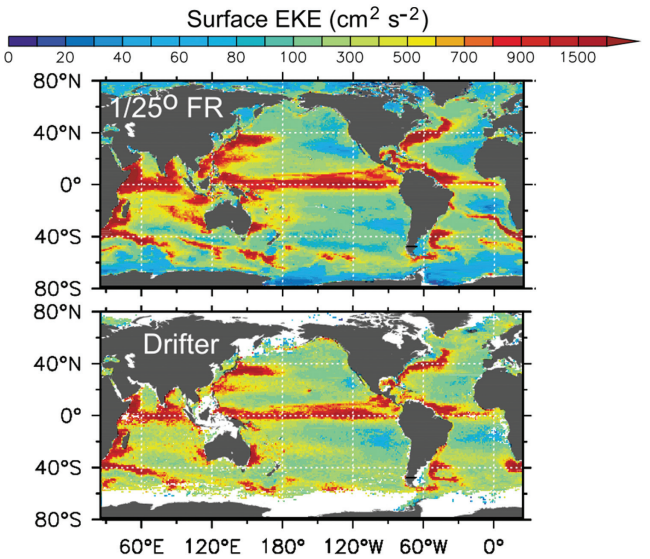

Figure 7. The eddy kinetic energy from a 1/25° numerical model (top) and from historical drifter observations (bottom). Local maxima in energy are associated with the western boundary currents such as the Gulf Stream. High energy also occurs along the equator. Though the energy outside these areas is lower, eddies are a persistent feature throughout the globe. Image courtesy P Thoppil.

over time. For values of $U_0 = 0.1$ m/s, $H = 1000$ m, $f_0 = 10^{-4}$ 1/s, the wavelength of the most rapidly growing instability is 391 km. The scale is comparable to the size of mesoscale eddies in Figure 1, though the eddies are smaller for many reasons. This simple linear analysis only describes the beginning of the process through which perturbations grow in amplitude and lead to formation of ocean eddies. The vertical structure of the perturbations is very important. The perturbation analysis shows that features in the deep ocean are shifted to the east relative to features in the surface. This sets up the flow necessary to lead to the instability.

The initial formation moves the warm southern waters to the north and cold northern waters to the south, which reduces the slope of the isotherm planes. The effect is to transfer the available potential energy stored in the thermocline into kinetic energy of the eddy field. As the process proceeds, the linear assumptions in the derivation here are no longer valid, otherwise the perturbation would grow unbounded. Instead, meanders in the currents form into closed circulations that leave the relatively cold core eddies south of the Gulf Stream and warm core eddies north of the Gulf Stream as seen in Figure 1.

Although the available energy is large in the Gulf Stream and the associated eddies are very strong, this process is by no means restricted to only the strong currents across which large slopes in isotherms exist. One example from Thoppil, Richman, and Hogan (2011) is shown in Figure 7. Eddy kinetic energy is the time average of the kinetic energy after

removing the mean velocity field. We see areas of strong western boundary currents contain very high variability in the kinetic energy, and the ocean interior is still affected by the influence of eddies. Mesoscale eddies form throughout the global oceans, and the ocean variability at 100 km scales is typically dominated by the mesoscale eddy field.

The growth of instabilities in the ocean currents leads to a difficult ocean prediction problem. The ocean mesoscale field prediction problem is similar to the prediction of atmospheric weather. Small perturbations grow in time. Given an accurate initial condition that reflects the position of mesoscale eddies, small errors result in a numerical forecast diverging from reality at some point in time at which the forecast has no skill in predicting the actual locations of eddies. The implication is that continual observations are required to correct the initial condition on a regular basis, and the vast majority of information for the ocean mesoscale is provided by satellite altimeters. Predictive skill has been demonstrated out to 30 days (Metzger et al. 2014). Achieving this skill requires accuracy in the numerical model as well as low latency access to global data sets and appropriate methods to correct initial conditions for forecasts. Because nonlinear processes are required in the development of mesoscale eddies, numerical model resolution must also be relatively high (Hurlburt et al. 2011).

12. Frontogenesis

Eddies shed from the Gulf Stream contain water masses that are quite different from the surrounding waters. Even eddies forming away from strong currents contain water masses that differ from their surroundings. Thus, strong buoyancy gradients exist across the periphery of eddies. The thermal wind equation (27) indicates that there must be horizontal density gradients to balance the vertical velocity gradients. In addition, the eddy currents continually drive waters of different buoyancy into confluence. The resulting effect is seen in Figure 1 as thin filaments of different temperature water wrapping around the mesoscale features and, also, along the Gulf Stream. The mesoscale field drives confluence of water that then leads to a secondary circulation in the vertical referred to as frontogenesis. This is a process in the atmosphere that leads to sharpening of fronts, and, in the ocean, it serves as a mechanism for upwelling and downwelling around eddies. This process is predictable to an extent if the ocean eddy locations and water masses are accurately predicted.

Consider how a 2D flow would change the density gradients of a material element. This can be done by taking the x and y derivatives of the conservation equation for density (32).

$$\frac{D}{Dt}\left(\frac{\partial \rho}{\partial x}, \frac{\partial \rho}{\partial y}\right) = \left(-u_x \frac{\partial \rho}{\partial x} - v_x \frac{\partial \rho}{\partial y}, -u_y \frac{\partial \rho}{\partial x} - v_y \frac{\partial \rho}{\partial y}\right) = \left(Q_x, Q_y\right) \tag{65}$$

As an example, consider a 2D flow of $(u, v) = (-x, y)$, which is nondivergent, having a zonal velocity moving toward the $x = 0$ line and a meridional velocity moving away from the $y = 0$ line. Material along the $x = 0$ line is being stretched in the y direction while being compressed in the x direction without changing area. If the initial buoyancy field is a

simply $\rho = x$, we see that the confluence along $x = 0$ is increasing the horizontal buoyancy gradient. The rate at which this is occurring is given by the vector Q.

Returning to the nondimensional equations (56), ignoring the effects of β and ignoring the order 1 pressure gradient, the order 1 velocity can be diagnosed from the total derivative of the order 0 geostrophic velocity field:

$$\left(\frac{\partial}{\partial t} + u_0\frac{\partial}{\partial x} + v_0\frac{\partial}{\partial y}\right)v_0 - f_o u_1 = 0 \tag{66}$$

The order 1 quasigeostrophic conservation of density equation is

$$\left(\frac{\partial}{\partial t} + u_0\frac{\partial}{\partial x} + v_0\frac{\partial}{\partial y}\right)\rho' + \frac{\rho_o}{g}N^2 w_1 = 0 \tag{67}$$

These two are combined through the thermal wind equation (27) relating horizontal density gradients to vertical velocity gradients to provide the relation between the vertical and horizontal order 1 velocities:

$$\frac{\rho_o f_o^2}{g}\frac{\partial u_1}{\partial z} + \frac{\rho_o}{g}N^2\frac{\partial w_1}{\partial x} = 2Q_x \tag{68}$$

A similar equation may be constructed for Q_y. For the case at hand, consider simple 2D confluence described by $(u_0, v_0) = (-x, y)$ and density $\rho' = x$ so that $Q = (1, 0)$. By introducing the stream function in the vertical x, z plane so that

$$\left(\frac{\rho_o f_o^2}{g}u_1, \frac{\rho_o}{g}N^2 w_1\right) = \left(\frac{\partial\psi}{\partial z}, \frac{\partial\psi}{\partial x}\right) \tag{69}$$

It is evident that (69) becomes the Poisson equation $\partial^2\psi/\partial z^2 + \partial^2\psi/\partial x^2 = 2Q_x$. Consider a view in the x, z plane. The confluence front is oriented in the y direction, and the confluence creates increasing density gradients. This produces a positive Q_x, which in turn drives a circulation in the plane perpendicular to the front. The circulation has upward motion on the less dense (warm) side of the front and downward motion on the more dense (cold) side of the front. This overturning circulation occurs along the periphery of the mesoscale eddies. It is in these areas where eddies drive confluence of different density water masses together. The vertical circulation within the frontogenesis brings deeper colder waters near the surface and produces many of the fine filament features seen in Figure 1. The surface mixed layer becomes thinner on the upwelling side of the front (Figure 8). The frontogenesis mechanism shown here is only one of many generation mechanisms leading to vertical circulation near the surface. These features become important in operational applications where biological productivity is strongly affected by the upwelling of nutrient rich deep waters. Fishing fleets work to minimize operational costs and direct efforts to areas of greatest expected return. Prediction of these areas leads to reduced costs.

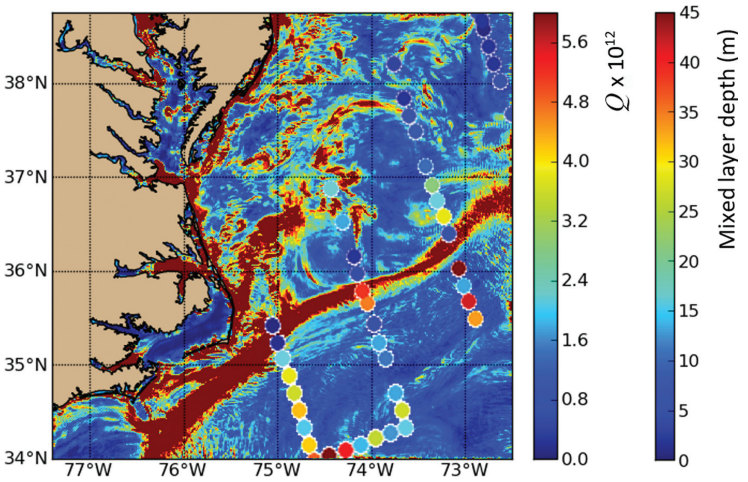

Figure 8. The colored background is the Q vector magnitude computed from a numerical model. The colored dots indicate a mixed layer observed on 12 July 2013 by aircraft-dropped, expendable bathythermograph instruments. In the northeastern domain, the thin mixed layer dominates. South of the Gulf Stream, deeper mixed layers dominate. On the edge of the Gulf Stream, in areas of high Q, very thin mixed layers are consistently observed. Data courtesy of J Richman.

13. The zoo of surface phenomena

Although many of the processes at the ocean surface are parameterized, some of the largest features—those that occupy the submesoscale—are beginning to be resolved in operational models. This requires resolutions of 1 km or higher (Capet et al. 2008), which are being reached in regional operational systems (Rowley and Mask 2014). The submesoscale is distinguished in the previous equations by order unity Rossby and Froude numbers, which means that few of the approximations made here can be made generally on these length scales. As such, a diverse set of phenomena occupy these scales, as reviewed by Thomas, Tandon, and Mahadevan (2008) and McWilliams (2016). Because waves, winds, and convection mix the upper ocean, the stratification is low, which allows for significantly smaller baroclinic instability and eddies than elsewhere (Boccaletti, Ferrari, and Fox-Kemper 2007).

On smaller scales, geostrophy, stratification, and even hydrostasy give way to active waves and turbulence. In modeling many of these boundary layers, individual features are rarely resolved. Instead, budgets of energy, temperature, and salinity can be used to constrain processes (Kraus and Turner 1967), or similarity theories for turbulence can be applied (Large, McWilliams, and Doney 1994). Scaling laws and balances, such as those for the turbulent Ekman depth or the Monin–Obukhov depth balancing shear and convection, are used in devising these schemes. Recent work has emphasized the role of waves in driving turbulence (McWilliams, Sullivan, and Moeng 1997; Belcher et al. 2012; Harcourt 2013) and improved air-sea fluxes (e.g., Liang et al. 2011; Fairall et al. 2011). Reviews (Burchard

et al. 2008; Sullivan and McWilliams 2009) and texts (Thorpe 2005; Baumert 2005) offer more depth than is possible here.

Finally, because they coexist in the boundary layer, submesoscale fronts and eddies, waves, phytoplankton, and turbulence may interact with one another. Understanding of these interactions is just beginning, but simulations (Hamlington et al. 2014; Smith, Hamlington, and Fox-Kemper 2015; Suzuki and Fox-Kemper 2016; Taylor and Ferrari 2010), theory (Haney et al. 2015; McWilliams et al. 2012), observations (D'Asaro et al. 2011; Mahadevan et al. 2012), and new parameterizations (Fox-Kemper, Ferrari, and Hallberg 2008) are contributing in this rapidly developing area.

14. Application of dynamical insights to operational oceanography

We began this chapter with a single image of the Gulf Stream region and many local ocean features. It should be recognized that this single image in and of itself is a tremendous achievement in the field of oceanography requiring years of development of satellite programs and many years of development of the ability to process and analyze such observations. The considerations in this chapter are enabled by several decades of effort to observe the ocean in innovative ways. Finally, the great insight from many creative and critical thinkers have provided dynamical relations to the features we see in many observations acquired within the ocean. We build operational ocean predictions on all this prior insight provided by a vast range of researchers and practitioners. In this chapter we have provided an examination of some of the ocean processes involved in the features we observe in Figure 1. There are several considerations the reader should keep in mind moving forward from this point.

The operational oceanography practitioner should realize that our dynamical understanding is insufficient. Enormous strides in understanding have brought the science and operational communities to the point at which they have enabled operational forecasts of the ocean. Global operational ocean predictions began in earnest just before 2000, and thus this is a relatively new area. Our forecasts continually fall short. This is demonstrated in several ways. Misforecast positions of ocean features are commonplace. A small error in positioning a mesoscale feature drastically changes the forecast pathways of transport for material contaminants, and evaluations of system performance show that predicting velocities and implied trajectories is difficult (Blockley, Martin, and Hyder 2012; Barron et al. 2007). Equally concerning is the operational ability to provide future decision information. The inability to forecast conditions prevents many endeavors requiring high-level societal policy decisions, including harvesting clean energy from the oceans, establishing sustainable aquaculture, determining hypoxic areas affected by agricultural utilization, and preparing ourselves for future possible changes in the Earth environment. The lack of present ability to predict the ocean limits decisions within these areas.

To address these shortfalls requires continued understanding of the ocean dynamics and exploitation in operational systems. A significant obstacle is that these activities often occur

in different groups or departments, or even agencies, of a government. Interaction is necessary between the operational center providing predictions and the researchers developing the next system. The operational centers receive regular feedback on performance for many applications. The researchers develop the knowledge of potential shortfalls necessary to meet required performance. These interactions form the basis of operations-to-research and research-to-operations efforts. The components of research and operations too easily drift into their own spheres of consideration, and constant effort is required to align the two (Bernardet et al. 2015)

Application of ocean dynamics affects the future of our society. Understanding of ocean dynamics continues to evolve. New scientific results continue to be published that must be considered to build future prediction capabilities. It is incumbent on the operational oceanography practitioner to remain abreast of developments in ocean dynamics. The operational practitioner must continually maintain current knowledge and apply new dynamical understanding to meet existing and future prediction requirements.

Acknowledgments. This research is funded by a grant from BP/The Gulf of Mexico Research Initiative to the Consortium for Advanced Research on the Transport of Hydrocarbon in the Environment (CARTHE) and the project Submesoscale Prediction of Eddies through Altimeter Retrieval supported by the Office of Naval Research (Program Element 062435N). This is contribution NRL/JA/7320—11-1001 and has been approved for public release.

REFERENCES

Barnston, A. G., M. K. Tippett, M. L. L'Heureux, S. Li, and D. G. DeWitt. 2012. Skill of real-time seasonal ENSO model predictions during 2002–11: Is our capability increasing? Bull. Am. Meteorol. Soc., *93*(5), 631–651. doi: 10.1175/BAMS-D-11-00111.1

Barron, C. N., L. F. Smedstad, J. M. Dastugue, and O. M. Smedstad. 2007. Evaluation of ocean models using observed and simulated drifter trajectories: Impact of sea surface height on synthetic profiles for data assimilation. J. Geophys. Res.: Oceans, *112*(C7), C07019. doi: 10.1029/2006JC003982

Baumert, H. Z. 2005. Marine Turbulence: Theories, Observations, and Models, vol. 1. Cambridge: Cambridge University Press, 672 pp.

Belcher, S. E., A. L. M. Grant, K. E. Hanley, B. Fox-Kemper, L. Van Roekel, P. P. Sullivan, W. G. Large et al. 2012. A global perspective on Langmuir turbulence in the ocean surface boundary layer. Geophys. Res. Lett., *39*(18), L18605. doi: 10.1029/2012GL052932

Bernardet, L., V. Tallapragada, S. Bao, S. Trahan, Y. Kwon, Q. Liu, M. Tong et al. 2015. Community support and transition of research to operations for the hurricane weather research and forecasting model. Bull. Am. Meteorol. Soc., *96*(6), 953–960. doi: 10.1175/BAMS-D-13-00093.1

Blockley, E. W., M. J. Martin, and P. Hyder. 2012. Validation of FOAM near-surface ocean current forecasts using Lagrangian drifting buoys. Ocean Sci., *8*(4), 551–565. doi:10.5194/os-8-551-2012

Boccaletti, G., R. Ferrari, and B. Fox-Kemper. 2007. Mixed layer instabilities and restratification. J. Phys. Oceanogr., *37*(9), 2228–2250. doi: 10.1175/JPO3101.1

Buijsman, M. C., Y. Uchiyama, J. C. McWilliams, and C. R. Hill-Lindsay. 2012. Modeling semidiurnal internal tide variability in the Southern California Bight. J. Phys. Oceanogr., *42*(1), 62–77. doi: 10.1175/2011JPO4597.1

Burchard, H., P. D. Craig, J. R. Gemmrich, H. van Haren, P.-P. Mathieu, H. E. Markus Meier, W. A. M. Nimmo Smith et al. 2008. Observational and numerical modeling methods for quantifying coastal ocean turbulence and mixing. Prog. Oceanogr., *76*(4), 399–442. doi: 10.1016/j.pocean.2007.09.005

Callies, J. and R. Ferrari. 2013. Interpreting energy and tracer spectra of upper-ocean turbulence in the submesoscale range (1–200 km). J. Phys. Oceanogr., *43*(11), 2456–2474. doi: 10.1175/JPO-D-13-063.1

Capet, X., J. C. Mcwilliams, M. J. Mokemaker, and A. F. Shchepetkin. 2008. Mesoscale to submesoscale transition in the California current system. Part I: Flow structure, eddy flux, and observational tests. J. Phys. Oceanogr., *38*(1), 29–43. doi: 10.1175/2007JPO3671.1

Charney, J. G. 1947. The dynamics of long waves in a baroclinic westerly current. J. Meteorol., *4*, 136–162. doi: 10.1175/1520-0469(1947)004<0136:TDOLWI>2.0.CO;2

Chavanne, C. P. and P. Klein. 2015. Quasigeostrophic diagnosis of mixed-layer dynamics embedded in a mesoscale turbulent field. J. Phys. Oceanogr., *46*, 275–287. doi: 10.1175/JPO-D-14-0178.1

Chelton, D. B., R. A. Deszoeke, M. G. Schlax, K. El Naggar, and N. Siwertz. 1998. Geographical variability of the first baroclinic Rossby radius of deformation. J. Phys. Oceanogr., *28*(3), 433–460. doi: 10.1175/1520-0485(1998)028<0433:GVOTFB>2.0.CO;2

Chelton, D. B., M. G. Schlax, and R. M. Samelson. 2011. Global observations of nonlinear mesoscale eddies. Prog. Oceanogr. *91*(2), 167–216. doi: 10.1016/j.pocean.2011.01.002

Craik, A. D. D. and S. Leibovich. 1976. A rational model for Langmuir circulations. J. Fluid Mech., *73*, 401–426. doi: 10.1017/S0022112076001420

Cushman-Roisin, B. and V. Malačič. 1997. Bottom Ekman pumping with stress-dependent eddy viscosity. J. Phys. Oceanogr., *27*(9), 1967–1975. doi: 10.1175/1520-0485(1997)027<1967:BEPWSD>2.0.CO;2

D'Asaro, E., C. Lee, L. Rainville, R. Harcourt, and L. Thomas. 2011. Enhanced turbulence and energy dissipation at ocean fronts. Science, *332*, 318–322. doi: 10.1126/science.1201515

Danabasoglu, G., S. C. Bates, B. P. Briegleb, S. R. Jayne, M. Jochum, W. G. Large, S. Peacock, and S. G. Yeager. 2012. The CCSM4 ocean component. J. Clim., *25*(5), 1361–1389. doi: 10.1175/JCLI-D-11-00091.1

Dunne, J. P., J. G. John, A. J. Adcroft, S. M. Griffies, R. W. Hallberg, E. Shevliakova, R. J. Stouffer et al. 2012. GFDL's ESM2 global coupled climate–carbon earth system models. Part I: Physical formulation and baseline simulation characteristics. J. Clim., *25*(19), 6646–6665. doi: 10.1175/JCLI-D-11-00560.1

Eady, E. T. 1949. Long waves and cyclone waves. Tellus, *1*(3), 33–52. doi: 10.1111/j.2153-3490.1949.tb01265.x

Early, J. J., R. M. Samelson, and D. B. Chelton. 2011. The evolution and propagation of quasigeostrophic ocean eddies. J. Phys. Oceanogr., *41*(8), 1535–1555. doi: 10.1175/2011JPO4601.1

Egbert, G. D. and R. D. Ray. 2000. Significant dissipation of tidal energy in the deep ocean inferred from satellite altimeter data. Nature, *405*(6788), 775–778. doi: 10.1038/35015531

Fairall, C. W., M. Yang, L. Bariteau, J. B. Edson, D. Helmig, W. McGillis, S. Pezoa et al. 2011. Implementation of the Coupled Ocean-Atmosphere Response Experiment flux algorithm with CO2, dimethyl sulfide, and O3. J. Geophys. Res.: Oceans, *116*(C4), C00F09. doi: 10.1029/2010JC006884

Feistel, R. 2008. A Gibbs function for seawater thermodynamics for −6 to 80°C and salinity up to 120 g kg–1. Deep Sea Res., Part I, *55*, 1639–1671. doi: 10.1016/j.dsr.2008.07.004

Fox-Kemper, B. S. Bachman, B. Pearson, and S. Reckinger. Principles and advances in subgrid modeling for eddy-rich simulations. CLIVAR Exchanges, *19*(2):42–46, July 2014.

Fox-Kemper, B., R. Ferrari, and R. Hallberg. 2008. Parameterization of mixed layer eddies. Part I: Theory and diagnosis. J. Phys. Oceanogr., *38*(6), 1145–1165. doi: 10.1175/2007JPO3792.1

Fox-Kemper, B., and D. Menemenlis. "Can large eddy simulation techniques improve mesoscale rich ocean models?." Ocean modeling in an eddying regime (2008): 319–337.

Fu, L.-L. and B. Qiu. 2002. Low-frequency variability of the North Pacific Ocean: The roles of boundary-and wind-driven baroclinic Rossby waves. J. Geophys. Res.: Oceans, *107*(C12), 3220. doi: 10.1029/2001JC001131

Gill, A. E. 1982. Atmosphere-Ocean Dynamics (International Geophysics). New York: Academic Press. 662 pp.

Haidvogel, D. B., E. N. Curchitser, S. Danilov and B. Fox-Kemper, 2017. Numerical Modelling in a Multi-Scale Ocean. In The Sea: The Science of Ocean Prediction, special issue, J. Mar. Res., in press.

Hamlington, P. E., L. P. Van Roekel, B. Fox-Kemper, K. Julien, and G. P. Chini. 2014. Langmuir–submesoscale interactions: Descriptive analysis of multiscale frontal spindown simulations. J. Phys. Oceanogr., *44*(9), 2249–2272. doi: 10.1175/JPO-D-13-0139.1

Haney, S., B. Fox-Kemper, K. Julien, and A. Webb. 2015. Symmetric and geostrophic instabilities in the wave-forced ocean mixed layer. J. Phys. Oceanogr., *45*(12), 3033–3056. doi: 10.1175/JPO-D-15-0044.1

Harcourt, R. R. 2013. A second-moment closure model of Langmuir turbulence. J. Phys. Oceanogr., 43(4), 673–697. doi: 10.1175/JPO-D-12-0105.1

Hermann, A. J., E. N. Curchitser, D. B. Haidvogel, and E. L. Dobbins. 2009. A comparison of remote vs. local influence of El Niño on the coastal circulation of the northeast Pacific. Deep Sea Res., Part II, *56*(24), 2427–2443. doi: 10.1016/j.dsr2.2009.02.005

Hurlburt, H. E., E. J. Metzger, J. G. Richman, E. P. Chassignet, Y. Drillet, M. W. Hecht, O. Le Galloudec et al. 2011. Dynamical evaluation of ocean models using the Gulf Stream as an example, *In* Operational Oceanography in the 21st Century, Schiller A., Brassington G., eds. Dordrecht: Springer, pp. 545–609.

Jayne, S. R. and L. C. St Laurent. 2001. Parameterizing tidal dissipation over rough topography. Geophys. Res. Lett., *28*(5), 811–814. doi: 10.1029/2000GL012044

Kantha, L. H. and C. A. Clayson. 1994. An improved mixed layer model for geophysical applications. J. Geophys. Res.: Oceans, *99*(C12), 25235–25266. doi: 10.1029/94JC02257

Kraus, E. B. and J. S. Turner. 1967. A one-dimensional model of the seasonal thermocline II. The general theory and its consequences. Tellus, *19*(1), 98–106. doi: 10.1111/j.2153-3490.1967.tb01462.x

Kug, J.-S., J. Choi, S.-I. An, F.-F. Jin, and A. T. Wittenberg. 2010. Warm pool and cold tongue El Niño events as simulated by the GFDL 2.1 coupled GCM. J. Clim. *23*(5), 1226–1239. doi: 10.1175/2009JCLI3293.1

Large, W. G., J. C. McWilliams, and S. C. Doney. 1994. Oceanic vertical mixing: A review and a model with a nonlocal boundary layer parameterization. Rev. Geophys., *32*(4), 363–403. doi: 10.1029/94RG01872

Liang, J.-H., J. C. McWilliams, P. P. Sullivan, and B. Baschek. 2011. Modeling bubbles and dissolved gases in the ocean. J. Geophys. Res.: Oceans, *116*(C3), C03015. doi: 10.1029/2010JC006579

MacCready, P. and G. Pawlak. 2001. Stratified flow along a corrugated slope: Separation drag and wave drag. J. Phys. Oceanogr., *31*(10), 2824–2839. doi: 10.1175/1520-0485(2001)031<2824:SFAACS>2.0.CO;2

Mahadevan, A., E. D'Asaro, C. Lee, and M. J. Perry. 2012. Eddy-driven stratification initiates North Atlantic spring phytoplankton blooms. Science *337*(6090), 54–58. doi: 10.1126/science.1218740

Marshall, J., C. Hill, L. Perelman, and A. Adcroft. 1997. Hydrostatic, quasi-hydrostatic, and nonhydrostatic ocean modeling. J. Geophys. Res.: Oceans, *102*(C3), 5733–5752. doi: 10.1029/96JC02776

McCreary, J. P. 1981. A linear stratified ocean model of the equatorial undercurrent. Philos. Trans. R. Soc., A, *298*(1444), 603–635. doi: 10.1098/rsta.1981.0002

McDougall, T. J., D. R. Jackett, D. G. Wright, and R. Feistel. 2003. Accurate and computationally efficient algorithms for potential temperature and density of seawater. J. Atmos. Ocean Technol., *20*(5), 730–741. doi: 10.1175/1520-0426(2003)20<730:AACEAF>2.0.CO;2

McWilliams, James C. "Submesoscale currents in the ocean." Proc. R. Soc. A 472, no. 2189 (2016): 20160117.

McWilliams, J. C. 1985. A uniformly valid model spanning the regimes of geostrophic and isotropic, stratified turbulence: Balanced turbulence. J. Atmos. Sci., *42*(16), 1773–1774. doi: 10.1175/1520-0469(1985)042<1773:AUVMST>2.0.CO;2

McWilliams, J. C., E. Huckle, J.-H. Liang, and P. P. Sullivan. 2012. The wavy Ekman layer: Langmuir circulations, breaking waves, and Reynolds stress. J. Phys. Oceanogr., *42*(11), 1793–1816. doi: 10.1175/JPO-D-12-07.1

McWilliams, J. C., P. P. Sullivan, and C.-H. Moeng. 1997. Langmuir turbulence in the ocean. J. Fluid Mech., *334*, 1–30. doi: 10.1017/S0022112096004375

Mellor, G. L. and T. Yamada. 1982. Development of a turbulence closure model for geophysical fluid problems. Rev. Geophys., *20*(4), 851–875. doi: 10.1029/RG020i004p00851

Metzger, E. J., O. M. Smedstad, P. G. Thoppil, H. E. Hurlburt, J. A. Cummings, A. J. Wallcraft, L. Zamudio et al. 2014. US Navy operational global ocean and Arctic ice prediction systems. Oceanography, *27*(3), 32–43. doi: 10.5670/oceanog.2014.66

MODE Group. 1978. The mid-ocean dynamics experiment. Deep Sea Res., *25*(10), 859–910. doi: 10.1007/978-94-007-0360-5_7

Niiler, P. P., N. A. Maximenko, and J. C. McWilliams. 2003. Dynamically balanced absolute sea level of the global ocean derived from near-surface velocity observations. Geophys. Res. Lett., *30*(22), 2164. doi: 10.1029/2003GL018628

Nikurashin, M. and R. Ferrari. 2010. Radiation and dissipation of internal waves generated by geostrophic motions impinging on small-scale topography: Theory. J. Phys. Oceanogr., *40*(5), 1055–1074. doi: 10.1175/2009JPO4199.1

Pedlosky, J. 2013. Geophysical fluid dynamics. Berlin Heidelberg: Springer Science and Business Media. 626 pp.

Pollard, R. T. and L. A. Regier. 1992. Vorticity and vertical circulation at an ocean front. J. Phys. Oceanogr., *22*(6), 609–625. doi: 10.1175/1520-0485(1992)022<0609:VAVCAA>2.0.CO;2

Pope, S. B. 2001. Turbulent flows. Cambridge: Cambridge University Press. 802 pp.

Qiu, B. and S. Chen. 2012. Multidecadal sea level and gyre circulation variability in the northwestern tropical Pacific Ocean. J. Phys. Oceanogr., *42*(1), 193–206. doi: 10.1175/JPO-D-11-061.1

Qiu, B., W. Miao, and P. Müller. 1997. Propagation and decay of forced and free baroclinic Rossby waves in off-equatorial oceans*. J. Phys. Oceanogr., *27*(11), 2405–2417. doi: 10.1175/1520-0485(1997)027<2405:PADOFA>2.0.CO;2

Ray, R. D. and D. E. Cartwright. 2001. Estimates of internal tide energy fluxes from Topex/Poseidon altimetry: Central North Pacific. Geophys. Res. Lett., *28*(7), 1259–1262. doi: 10.1029/2000GL012447

Ray, R. D. and E. D. Zaron. 2011. Non-stationary internal tides observed with satellite altimetry. Geophys. Res. Lett., *38*(17), L17609. doi: 10.1029/2011GL048617

Richman, J. G., C. Wunsch, and N. G. Hogg. 1977. Space and time scales of mesoscale motion in the western North Atlantic. Rev. Geophys., *15*(4), 385–420. doi: 10.1029/RG015i004p00385

Robinson, A. R. and J. C. McWilliams. 1974. The baroclinic instability of the open ocean. J. Phys. Oceanogr., *4*(3), 281–294. doi: 10.1175/1520-0485(1974)004<0281:TBIOTO>2.0.CO;2

Rowley, C. and A. Mask. 2014. Regional and coastal prediction with the relocatable ocean nowcast/forecast system. Oceanography, *27*, 44–55. doi: 10.5670/oceanog.2014.67

Shriver, J. F., B. K. Arbic, J. G. Richman, R. D. Ray, E. J. Metzger, A. J. Wallcraft, and P. G. Timko. 2012. An evaluation of the barotropic and internal tides in a high-resolution global ocean circulation model. J. Geophys. Res.: Oceans, *117*(C10), C10024. doi: 10.1029/2012JC008170

Simmons, H. L., R. W. Hallberg, and B. K. Arbic. 2004. Internal wave generation in a global baroclinic tide model. Deep Sea Res., Part II, *51*(25), 3043–3068. doi: 10.1016/j.dsr2.2004.09.015

Smith, K. S. 2007. The geography of linear baroclinic instability in Earth's oceans. J. Mar. Res., *65*(5), 655–683. doi: 10.1357/002224007783649484

Smith, K. M., P. E. Hamlington, and B. Fox-Kemper. 2015. Effects of submesoscale turbulence on ocean tracers. J. Geophys. Res.: Oceans, *121*, 908–933. doi: 10.1002/2015JC011089

Smith, R. N., Y. Chao, P. P. Li, D. A. Caron, B. H. Jones, and G. S. Sukhatme. 2010. Planning and implementing trajectories for autonomous underwater vehicles to track evolving ocean processes based on predictions from a regional ocean model. Int. J. Rob. Res., *29*(12), 1475–1497. doi: 10.1177/0278364910377243

Spall, M. A. 2000. Generation of strong mesoscale eddies by weak ocean gyres. J. Mar. Res., *58*(1), 97–116. doi: 10.1357/002224000321511214

Sullivan, P. P. and J. C. McWilliams. 2009. Dynamics of winds and currents coupled to surface waves. Annu. Rev. Fluid. Mech., *42*, 19–42. doi: 10.1146/annurev-fluid-121108-145541

Suzuki, N. and B. Fox-Kemper. 2016. Understanding Stokes forces in the wave-averaged equations. Geophys. Res.: Oceans, *121*, 3579–3596. doi: 10.1002/2015JC011566

Taylor, J. R. and R. Ferrari. 2010. Buoyancy and wind-driven convection at mixed layer density fronts. J. Phys. Oceanogr., *40*(6), 1222–1242. doi: 10.1175/2010JPO4365.1

Thomas, L. N., A. Tandon, and A. Mahadevan. 2008. Submesoscale processes and dynamics. *In* Ocean Modeling in an Eddying Regime, M. Hecht and H. Hasumi, eds. Washington, DC: AGU Monograph, pp. 17–38.

Thoppil, P. G., J. G. Richman, and P. J. Hogan. 2011. Energetics of a global ocean circulation model compared to observations. Geophys. Res. Lett., *38*, L15607. doi: 10.1029/2011GL048347

Thorpe, S. A. 2005. The Turbulent Ocean. Cambridge: Cambridge University Press. 484 pp.

Tonani, M., M. Balmaseda, L. Bertino, E. Blockley, G. Brassington, F. Davidson, Y. Drillet et al. 2015. Status and future of global and regional ocean prediction systems. J. Oper. Oceanogr., *8*(Suppl 2), s201–s220. doi: 10.1080/1755876X.2015.1049892

Tsumune, D., T. Tsubono, M. Aoyama, and K. Hirose. 2012. Distribution of oceanic 137Cs from the Fukushima Dai-ichi Nuclear Power Plant simulated numerically by a regional ocean model. J. Environ. Radioact., *111*, 100–108. doi: 10.1016/j.jenvrad.2011.10.007

Vallis, G. K. 2006. Atmospheric and oceanic fluid dynamics: fundamentals and large-scale circulation. Cambridge: Cambridge University Press. 745 pp.

Warner, J. C., C. R. Sherwood, H. G. Arango, and R. P. Signell. 2005. Performance of four turbulence closure models implemented using a generic length scale method. Ocean Model., *8*(1), 81–113. doi: 10.1016/j.ocemod.2003.12.003

White, W. B. 1985. The resonant response of interannual baroclinic Rossby waves to wind forcing in the eastern midlatitude North Pacific. J. Phys. Oceanogr., *15*(4), 403–415. doi: 10.1175/1520-0485(1985)015<0403:TRROIB>2.0.CO;2

Williams, P. and P. Terawasi. 2011. Overview of tuna fisheries in the western and central Pacific Ocean, including economic conditions–2010. WCPFC-SC7-2011/GN WP-1.

Zhang, Z., O. B. Fringer, and S. R. Ramp. 2011. Three-dimensional, nonhydrostatic numerical simulation of nonlinear internal wave generation and propagation in the South China Sea. J. Geophys. Res.: Oceans, *116*(C5), C05022. doi: 10.1029/2010JC006424

Received: *2 May 2015*; revised: *28 May 2017*.

Editor's note: Contributions to *The Sea: The Science of Ocean Prediction* are being published separately in special issues of *Journal of Marine Research* and will be made available in a forthcoming supplement as Volume 17 of the series.